Mon. Not. R. Astron. Soc. **379,** 1571–1588 (2007) doi:10.1111/j.1365-2966.2007.12036.x

The SCUBA Half Degree Extragalactic Survey – IV. Radio–mm–FIR photometric redshifts

Itziar Aretxaga,[1⋆] David H. Hughes,[1] Kristen Coppin,[2,3] Angela M. J. Mortier,[4,5] Jeff Wagg,[1,6] James S. Dunlop,[4] Edward L. Chapin,[3] Stephen A. Eales,[7] Enrique Gaztañaga,[1,8] Mark Halpern,[3] Rob J. Ivison,[9] Eelco van Kampen,[10] Douglas Scott,[3] Stephen Serjeant,[11] Ian Smail,[2] Thomas Babbedge,[12] Andrew J. Benson,[13] Scott Chapman,[13] David L. Clements,[12] Loretta Dunne,[14] Simon Dye,[7] Duncan Farrah,[15] Matt J. Jarvis,[16,17] Robert G. Mann,[4] Alexandra Pope,[3] Robert Priddey,[18] Steve Rawlings,[17] Marc Seigar,[19] Laura Silva,[20] Chris Simpson[21] and Mattia Vaccari[12,22]

[1]*Instituto Nacional de Astrofísica, Óptica y Electrónica (INAOE), Aptdo. Postal 51 y 216, 72000 Puebla, Pue., Mexico*
[2]*Institute for Computational Cosmology, Durham University, South Road, Durham DH1 3LE*
[3]*Department of Physics & Astronomy, University of British Columbia, 6224 Agricultural Road, Vancouver, B.C., V6T 1Z1, Canada*
[4]*SUPA (Scottish Universities Physics Alliance), Institute for Astronomy, University of Edinburgh, Blackford Hill, Edinburgh EH9 3HJ*
[5]*Center for Astrophysics and Planetary Science, School of Physical Sciences, University of Kent, Canterbury CT2 7NR*
[6]*National Radio Astronomy Observatory, PO Box O, Socorro, NM 87801, USA*
[7]*Cardiff School of Physics and Astronomy, Cardiff University 5, The Parade, Cardiff CF24 3YB*
[8]*Institut d'Estudis Espacials de Catalunya, IEEC/CSIC, c/ Gran Capità 2-4, 08034 Barcelona, Spain*
[9]*UK ATC, Royal Observatory, Blackford Hill, Edinburgh EH9 3HJ*
[10]*Institute for Astrophysics, University of Innsbruck, Technikerstr. 25, A-6020, Innsbrusk, Austria*
[11]*Astrophysics Group, Department of Physics, The Open University, Milton Keynes, MK7 6AA*
[12]*Astrophysics Group, Blackett Laboratory, Imperial College, Prince Consort Rd., London SW7 2BW*
[13]*Caltech, 1200 E. California Blvd., Pasadena, CA 91125-0001, USA*
[14]*The School of Physics and Astronomy, University of Nottingham, University Park, Nottingham NG7 2RD*
[15]*Department of Astronomy, Cornell University, Space Sciences Building, Ithaca, NY 14853, USA*
[16]*Centre for Astrophysics Research, Science & Technology Research Institute, University of Hertfordshire, Hatfield AL10 9AB*
[17]*Department of Astrophysics, Denys Wilkinson Building, Keble Road, Oxford OX1 3RH*
[18]*Department of Physics, Astronomy & Mathematics, University of Herdfordshire, College Lane, Hatfield, Hertfordshire AL10 9AB*
[19]*Center for Cosmology, Department of Physics & Astronomy, Univ. of California, Irvine, 4129 Frederick Reines Hall, Irvine, CA 92697-4575, USA*
[20]*Osservatorio Astronomico di Trieste, Via Tiepolo 11, I-341311, Trieste, Italy*
[21]*Astrophysics Research Institute, Liverpool John Moores University, Twelve Quays House, Egerton Wharf, Birkenhead CH41 1LD*
[22]*Department of Astronomy, University of Padova, Vicolo dell'Osservatorio 2, I-35122, Padova, Italy*

Accepted 2007 May 27. Received 2007 May 11; in original form 2007 February 19

ABSTRACT

We present the redshift distribution of the Submillimetre Common-User Bolometer Array (SCUBA) Half Degree Survey (SHADES) galaxy population based on the rest-frame radio–mm–far-infrared (FIR) colours of 120 robustly detected 850 μm sources in the Lockman Hole East (LH) and Subaru *XMM–Newton* Deep Field (SXDF). The redshift distribution derived from the full spectral energy distribution (SED) information is shown to be narrower than that determined from the radio–sub-mm spectral index, as more photometric bands contribute to a higher redshift accuracy. The redshift distribution of sources derived from at least two photometric bands peaks at $z \approx 2.4$ and has a near-Gaussian distribution, with 50 per cent (interquartile range) of sources at $z = 1.8$–3.1. We find a statistically significant difference between the measured redshift distributions in the two fields; the SXDF peaking at a slightly lower redshift (median $z \approx 2.2$) than the LH (median $z \approx 2.7$), which we attribute to the noise properties of the radio observations. We demonstrate, however, that there could also be

⋆E-mail: itziar@inaoep.mx

field-to-field variations that are consistent with the measured differences in the redshift distributions and, hence, that the incomplete area observed by SHADES with SCUBA, despite being the largest sub-mm survey to date, may still be too small to fully characterize the bright sub-mm galaxy population. Finally, we present a brief comparison with the predicted, or assumed, redshift distributions of sub-mm galaxy formation and evolution models, and we derive the contribution of these SHADES sources and the general sub-mm galaxy population to the star formation rate density at different epochs.

Key words: surveys – galaxies: evolution – cosmology: miscellaneous – infrared: galaxies – submillimetre.

1 INTRODUCTION

The SCUBA Half Degree Survey (SHADES; Dunlop 2005; Mortier et al. 2005) was originally designed with the aim of characterizing the star formation history (Hughes et al. 2002) and clustering properties (van Kampen et al. 2005) of the bright end of the luminous dust-enshrouded galaxy population. To achieve these goals, we mapped two regions of the sky centred on the Lockman Hole East (LH) and Subaru *XMM–Newton* Deep Field (SXDF) with the Submillimetre Common-User Bolometer Array (SCUBA; Holland et al. 1999). With a proposed 1σ sensitivity of 2 mJy at 850 μm, the complete survey was predicted to identify a statistically robust sample of ∼200 galaxies, with sufficient radio-to-FIR ancillary data to help identify optical/infrared (IR) counterparts and derive spectroscopic/photometric redshifts. This redshift information is essential for determining the star formation and clustering properties for the whole population of ultraluminous dust-enshrouded galaxies. SCUBA was de-commissioned in mid-2005 having covered ∼40 per cent of the originally proposed area of the SHADES.[1]

Paper I of this series (Mortier et al. 2005) describes the survey motivation, strategy and the philosophy adopted for the analysis. Paper II (Coppin et al. 2006) presents the catalogue and number counts derived from the 850-μm sources. Paper III (Ivison et al. 2007) describes the identification of radio and mid-IR counterparts of these sources. This paper (Paper IV) constructs the redshift distribution derived from the radio–mm–FIR photometry of the SHADES sources based on a compilation of the 850 and 450 μm SCUBA data (Coppin et al. 2006), 1.4 GHz Very Large Array photometry (Ivison et al. 2007) and other previously published mm-to-FIR photometric observations towards these fields. A study of the mid-IR to optical properties of the SHADES population, and further constraints on the photometric redshifts of the sources, will be published elsewhere (Clements et al., in preparation; Dye et al., in preparation; Serjeant et al., in preparation). A spectroscopic study of a subsample of SHADES sources with identified optical/IR counterparts (Blain et al., in preparation) will also provide an important comparison of spectroscopic and photometric redshifts.

The cosmological parameters adopted throughout this paper are $H_0 = 71\ \mathrm{km\,s^{-1}\,Mpc^{-1}}$, $\Omega_\mathrm{M} = 0.27$ and $\Omega_\Lambda = 0.73$.

2 PHOTOMETRIC REDSHIFTS

Despite having mapped only ∼40 per cent of the planned 0.5 deg^2 area, SHADES remains the largest extragalactic sub-mm survey to date. The difficulties of following-up such large areas at other wavelengths, and hence the inhomogeneity of the multiwavelength data, implies that the same photometric-redshift technique cannot be applied to all sources. This section has been divided in two subsections: the first (Section 2.1) deals with the consideration of 850 μm and 1.4 GHz photometry which is available for all sources, and the use of the sub-mm–radio spectral index as a diagnostic of redshift; and the second (Section 2.2) describes the inclusion of additional photometry at 70 to 450 μm which is sufficiently sensitive to place important constraints on the radio–mm–FIR photometric redshifts for only a few tens of sources. In both sections, we make a brief introduction to the techniques used, the estimated uncertainties found when comparing photometric and spectroscopic redshifts for similar sub-mm galaxies, the results from the application of the techniques to individual SHADES sources and the combined redshift distributions derived for the entire SHADES population.

2.1 1.4 GHz/850 μm spectral index

2.1.1 Techniques and accuracies

One of the simplest redshift indicators for the sub-mm galaxy population is that formed by the ratio of the flux densities at 1.4 GHz and 850 μm. These wavebands trace the tight correlation between radio continuum emission, which is dominated by synchrotron radiation from supernova remnants, and thermal emission from warm dust heated by young stars (Helou, Soifer & Rowan-Robinson 1985; Condon 1992; Yun, Reddy & Condon 2001). This redshift indicator was systematically studied by Carilli & Yun (1999, 2000), and has been subsequently revised for different sub-mm galaxy sub-populations (Dunne, Clements & Eales 2000; Rengarajan & Takeuchi 2001). The 1.4 GHz to 850 μm flux-density ratio, or a spectral index derived from it, increases monotonically with redshift, with some degeneracy due to the variety of radio synchrotron slopes and mm-dust-emissivity indices present in the ISM of those local galaxies used to define the relationship. Additionally, there exists a level of degeneracy between the temperature of the dust generating the rest-frame FIR luminosity (and hence sub-mm flux) and the redshift. Regardless, by adopting a library of local galaxy templates, and accepting the intrinsic dispersion in their spectral energy distributions (SEDs), the 1.4 GHz to 850 μm flux-density ratio still provides a crude but useful estimation of the redshift. This indicator becomes relatively insensitive to redshift beyond $z \sim 3$, as the 850 μm filter starts to sample the flattening of the SED towards the rest-frame FIR peak, whilst still providing a powerful discriminant between low-redshift ($z < 2$) and high-redshift ($z > 2$) objects.

We will discuss the 1.4 GHz/850 μm spectral index following two different prescriptions: (i) the single-template maximum-likelihood technique originally designed by Carilli & Yun (1999, 2000),

[1] The complete 1800 arcmin^2 SHADES area towards the LH and the SXDF has recently been surveyed at the James Clerk Maxwell Telescope at 1.1 mm with AzTEC (Wilson et al. 2004), a continuum camera destined for the 50-m Large Millimetre Telescope (Serrano Pérez-Grovas et al. 2006). These AzTEC data are currently being analysed and the results will be presented elsewhere.

denoted as $z_{\rm phot}^{\rm CY}$ and (ii) a maximum-likelihood technique which simultaneously fits the 20 local templates of starbursts, ULIRGs and active galactic nuclei (AGN) used by Aretxaga et al. (2003) and Aretxaga, Hughes & Dunlop (2005), denoted as $z_{\rm phot}^{\rm A}$.

The success of any photometric-redshift technique is measured by the accuracy with which it can predict the individual redshifts for a sample of representative galaxies with known redshifts, which have not been used to define the method. Aretxaga, Hughes & Dunlop (2006) have previously assessed the accuracy of the above two 1.4 GHz/850 μm photometric-redshift indicators. Based on this study, we show in Fig. 1 a comparison of spectroscopic and photometric redshifts for 58 sub-mm or mm selected galaxies, complemented with a few objects selected at optical/FIR wavelengths, which have published optical/IR or CO spectroscopic redshifts and accompanying radio–FIR photometry. We will refer to this data set as the 'comparison sample' hereafter. This comparison study shows that the $z_{\rm phot}^{\rm A}$ prescription has a mean accuracy $\Delta z \equiv \langle |z_{\rm phot}^{\rm A} - z_{\rm spec}\,| \rangle \approx 0.65$ over the whole redshift interval, when one selects a robust sub-sample of objects with unambiguous optical/IR/radio counterparts and spectroscopic redshifts derived from the identification of two or more spectral lines. For the same robust sample of objects, $z_{\rm phot}^{\rm CY}$ has systematically larger errors, $\Delta z \approx 0.9$. This sample does not include powerful radio-loud AGN, for which the template SEDs used in the photometric-redshift analysis are not appropriate. The rms of the relation is $\langle\, (z_{\rm phot}^{\rm A} - z_{\rm spec})^2 \,\rangle^{1/2} \approx 0.8$. Restricting the analysis only to those galaxies with CO spectroscopic redshifts, the measured accuracy is $\Delta z \approx 0.6$ and has a rms of 0.8 at $0 \leqslant z \leqslant 4$. The precision degrades as the redshift increases, as expected from the 1.4 GHz/850 μm spectral index, which flattens beyond $z = 3$ (Carilli & Yun 2000), leading to a measured $\Delta z \approx 1.0$ at $3 \leqslant z \leqslant 4$. Using all objects with published photometry and spectroscopic redshifts, regardless of whether the associations that lead to the spectroscopic redshift are unambiguous or not, the overall accuracy over the $0 \leqslant z \leqslant 4$ regime degrades to $\Delta z \approx 0.8$ (see Aretxaga et al. 2006, fig. 1).

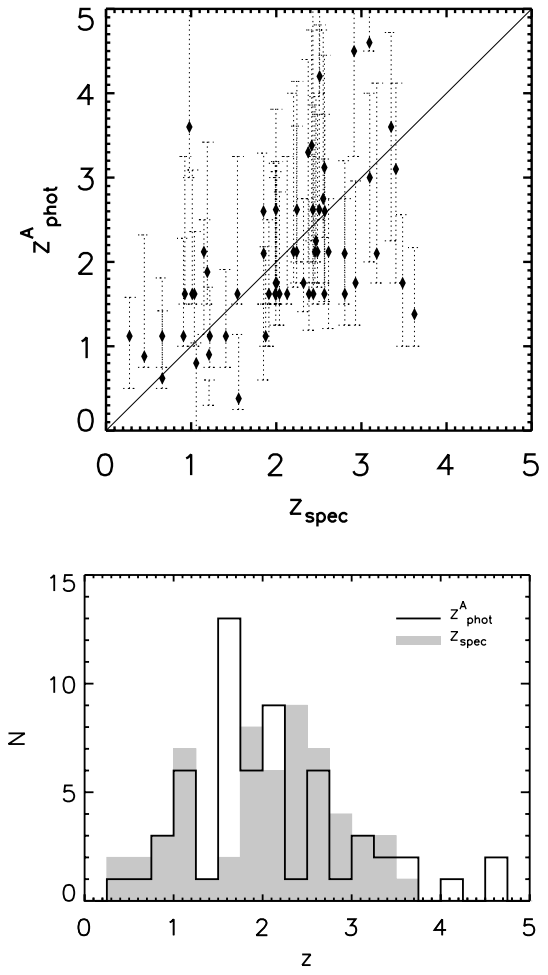

Figure 1. Top: comparison of spectroscopic and photometric redshifts derived from the 1.4 GHz/850 μm spectral index for a sample of 58 sub-mm galaxies with undisputed radio/optical/IR identifications, and spectroscopic redshifts derived from two or more lines (Aretxaga et al. 2006). The error bars represent 68 per cent confidence intervals in the determination of the redshift. The rms scatter of the relation $z_{\rm spec}$–$z_{\rm phot}^{\rm A}$ displayed is 0.8. Bottom: histogram distribution of the spectroscopic and photometric redshifts represented in the top panel, which illustrates the success in recovering the redshift distribution of the sample.

2.1.2 *The redshifts of SHADES sources*

The radio counterparts adopted for the photometric-redshift calculations of SHADES sources are the secure sample detected within 8 arcsec of the sub-mm position (Ivison et al. 2007), with a chance association probability between the radio and sub-mm source of $P < 0.05$. We have accepted some additional counterparts when a robustly detected radio source is still within 10 arcsec of the sub-mm centroid and, additionally, a 24 μm counterpart is associated with this radio identification. These extra radio counterparts are marked in the notes provided for each sub-mm source (see Tables 1 and 2), where we have calculated the corresponding P value of the radio association, which remains lower than 0.08. The 34 radio sources adopted as counterparts of SHADES galaxies in the LH field, and the 35 radio sources in the SXDF, have a combined chance association $P \approx 1.6$, and thus we expect to have incorrectly associated $\sim$1 of the SHADES sub-mm sources with a projected radio source.

For both techniques, the error bars of the photometric redshifts were derived by bootstrapping on the reported photometric and calibration errors (Coppin et al. 2006; Ivison et al. 2007), and are defined as the 68 per cent confidence interval of the resulting redshift probability distribution. The photometric error distributions used for the 850 μm photometry were derived by de-boosting the measured flux densities of the SCUBA sources. A de-boosting correction is necessary to provide a more accurate estimate of the flux of low signal-to-noise ratio (S/N) blank-field sources in sub-mm surveys, where the counts are typically very steep and faint galaxies can be statistically boosted above the nominal detection threshold. These errors are often non-Gaussian (see fig. 5 in Coppin et al. 2006). The 1.4 GHz flux densities do not need to be de-boosted, since this correction is dependent on the area defined by the search radius in identifying the source. In the case of finding associations within $\lesssim$8 arcsec radius around a known object, this is negligible. The error distributions for the 1.4 GHz flux densities were assumed to be Gaussian. In the case of $z_{\rm phot}^{\rm CY}$, the error estimated by Carilli & Yun (2000), to allow for a difference in templates, is added in quadrature to the errors derived by bootstrapping the photometry.

The probability distribution calculated for each source in this manner typically has a single peak, which broadens as the most probable redshift of the source increases. Fig. 2 shows an example of a typical solution derived from the use of 850 μm and 1.4 GHz photometry.

Table 1. Photometric redshifts for SHADES sources in the LH field based on the 1.4 GHz/850 μm spectral index. The columns give (1) name of the source; (2) $z^{\rm CY}_{\rm phot}$, photometric redshift using the prescription of Carilli & Yun (1999, 2000); (3) $z^{\rm A}_{\rm phot}$, photometric redshift using the template collection of Aretxaga et al. (2003, 2005), the 90 per cent confidence interval is given in parenthesis; (4) notes on which radio counterpart (from Ivison et al. 2007) is used in the computation of photo-z, in case of ambiguity (N for Northern component, S for Southern component, etc., or 'co-added' if the flux densities from all components are summed); and (5) $z_{\rm spec}$, spectroscopic redshift taken from the literature, where sources for which the redshifts are in parenthesis have reported ambiguities in their radio/optical counterpart associations, or where the redshifts are otherwise under scrutiny. The references for the spec-z (as a superscript of the values) and any debate about them (after the parenthesis, where it applies) are as follows: 1. Chapman et al. (2005); 2. Ivison et al. (2005); 3. Greve et al. (2005); 4. Chapman et al. (2003); 5. Swinbank (2005); 6. Chapman et al. (2002); 7. Almaini et al. (2005) and 8. Kovács et al. (2006).

Object	$z^{\rm CY}_{\rm phot}$	$z^{\rm A}_{\rm phot}$	Notes	$z_{\rm spec}$
SHADES J105201+572443 (Lock850.1)	$3.3 \pm {}^{1.8}_{1.2}$	$2.1 \pm {}^{2.0}_{0.1}$ (1.5–6.0)		$(2.148^{1,2})^2$
SHADES J105257+572105 (Lock850.2)	$5.1 \pm {}^{3.5}_{2.1}$	$3.1 \pm {}^{2.7}_{0.1}$ (2.2–7.0)	SW	
	$6.0 \pm {}^{4.0}_{2.5}$	$3.6 \pm {}^{1.7}_{0.6}$ (2.5–6.9)	NW	
SHADES J105257+572105 (Lock850.3)	$7.0 \pm {}^{4.4}_{3.3}$	$4.1 \pm {}^{1.6}_{0.6}$ (2.7–7.4)	S	$(3.036^{1})^2$
	$4.2 \pm {}^{2.8}_{1.6}$	$3.1 \pm {}^{1.6}_{0.8}$ (2.0–6.5)	Co-added	
SHADES J105204+572658 (Lock850.4)	$3.1 \pm {}^{1.6}_{1.1}$	$2.1 \pm {}^{1.8}_{0.4}$ (1.5–5.8)	Co-added	(0.526 or $1.482)^2$
SHADES J105302+571827 (Lock850.5)	$\geqslant 3.8$	$\geqslant 2.9$		
SHADES J105204+572526 (Lock850.6)	$7.3 \pm {}^{4.5}_{3.6}$	$4.1 \pm {}^{1.5}_{0.6}$ (3.0–7.8)		
SHADES J105301+572554 (Lock850.7)	$4.4 \pm {}^{3.0}_{1.8}$	$3.1 \pm {}^{1.8}_{0.6}$ (2.0–6.7)		
SHADES J105153+571839 (Lock850.8)	$\geqslant 3.0$	$\geqslant 2.5$		
SHADES J105216+572504 (Lock850.9)	$3.3 \pm {}^{1.8}_{1.2}$	$2.1 \pm {}^{2.0}_{0.1}$ (1.5–5.9)		1.85^{2}
SHADES J105248+573258 (Lock850.10)	$6.4 \pm {}^{0.7}_{2.1}$	$3.4 \pm {}^{2.3}_{0.6}$ (2.2–7.3)		
SHADES J105129+572405 (Lock850.11)	$\geqslant 2.7$	$\geqslant 2.3$		
SHADES J105227+572513 (Lock850.12)	$3.6 \pm {}^{2.2}_{1.5}$	$2.6 \pm {}^{1.7}_{0.6}$ (1.5–6.5)		$(2.142^{1})^2$
SHADES J105132+573134 (Lock850.13)	$\geqslant 2.6$	$\geqslant 1.5$		
SHADES J105230+572215 (Lock850.14)	$\geqslant 4.0$	$\geqslant 2.2$	No 1.4 GHz[a]	$2.611^{4,2}$
SHADES J105319+572110 (Lock850.15)	$3.5 \pm {}^{2.0}_{1.4}$	$2.6 \pm {}^{1.6}_{0.8}$ (1.1–6.0)	Co-added	
	$4.6 \pm {}^{3.2}_{2.1}$	$3.1 \pm {}^{1.9}_{0.9}$ (1.7–6.9)	S	
SHADES J105151+572637 (Lock850.16)	$2.3 \pm {}^{1.3}_{0.8}$	$1.6 \pm {}^{1.3}_{0.4}$ (1.0–4.7)		$(1.147^{1})^2$
SHADES J105158+571800 (Lock850.17)	$2.3 \pm {}^{1.2}_{0.8}$	$1.6 \pm {}^{1.2}_{0.4}$ (1.0–4.2)		$2.239^{1,2,3,5}$
SHADES J105227+572217 (Lock850.18)	$4.5 \pm {}^{3.2}_{1.8}$	$3.1 \pm {}^{2.1}_{0.6}$ (1.5–6.4)		$(1.956^{1})^4$
SHADES J105235+573119 (Lock850.19)	$\geqslant 2.4$	$\geqslant 1.7$		
SHADES J105256+573038 (Lock850.21)	$\geqslant 2.0$	$\geqslant 1.5$		
SHADES J105137+573323 (Lock850.22)	$\geqslant 2.8$	$\geqslant 2.0$		
SHADES J105213+573154 (Lock850.23)	$\geqslant 2.4$	$\geqslant 1.6$		
SHADES J105200+572038 (Lock850.24)	$3.0 \pm {}^{1.7}_{1.3}$	$2.6 \pm {}^{1.2}_{1.1}$ (1.1–5.8)		
SHADES J105240+572312 (Lock850.26)	$4.3 \pm {}^{3.0}_{2.0}$	$3.1 \pm {}^{1.8}_{1.1}$ (1.5–7.3)		
SHADES J105203+571813 (Lock850.27)	$5.1 \pm {}^{3.5}_{2.3}$	$3.4 \pm {}^{1.6}_{1.1}$ (2.0–6.7)		
SHADES J105257+573107 (Lock850.28)	$\geqslant 2.6$	$\geqslant 2.0$		
SHADES J105130+572036 (Lock850.29)	$\geqslant 2.8$	$\geqslant 2.2$		
SHADES J105207+571906 (Lock850.30)	$1.5 \pm {}^{0.8}_{0.6}$	$1.1 \pm {}^{0.8}_{0.4}$ (0.5–3.2)		2.692^{1}
SHADES J105216+571621 (Lock850.31)	$3.7 \pm {}^{2.2}_{1.5}$	$2.6 \pm {}^{1.9}_{0.6}$ (1.5–6.6)		
SHADES J105155+572311 (Lock850.33)	$2.7 \pm {}^{1.3}_{1.1}$	$1.9 \pm {}^{1.2}_{0.6}$ (1.2–5.2)		$(3.699,^{1}\ 2.686^{4,2})$
SHADES J105213+573328 (Lock850.34)	$4.9 \pm {}^{0.7}_{0.9}$	$3.4 \pm {}^{1.6}_{1.0}$ (2.0–6.5)		
SHADES J105246+572056 (Lock850.35)	$\geqslant 2.9$	$\geqslant 2.0$		
SHADES J105209+571806 (Lock850.36)	$\geqslant 3.4$	$\geqslant 2.8$		
SHADES J105124+572334 (Lock850.37)	$4.4 \pm {}^{0.9}_{1.4}$	$2.9 \pm {}^{1.6}_{1.1}$ (1.2–6.3)	N ($P = 0.013$)	
	$7.1^{1.8}_{1.6}$	$3.9 \pm {}^{2.6}_{1.1}$ (2.0–7.8)	Adopted $P = 0.078$	
SHADES J105307+572431 (Lock850.38)	$4.2 \pm {}^{2.1}_{1.6}$	$2.4 \pm {}^{1.6}_{1.1}$ (1.2–6.2)		
SHADES J105224+571609 (Lock850.39)	$\geqslant 3.1$	$\geqslant 2.5$		
SHADES J105202+571915 (Lock850.40)	$4.3 \pm {}^{3.1}_{2.0}$	$2.6 \pm {}^{2.0}_{0.6}$ (1.5–6.4)		
SHADES J105159+572423 (Lock850.41)	$2.9 \pm {}^{1.5}_{1.1}$	$2.1 \pm {}^{1.4}_{0.6}$ (1.3–5.3)	S	$(0.689^{1})^{6,2,7,8}$
	$2.4 \pm {}^{0.3}_{0.4}$	$1.4 \pm {}^{1.4}_{0.1}$ (1.0–4.7)	N+S	
SHADES J105257+572351 (Lock850.43)	$4.4 \pm {}^{3.2}_{2.1}$	$3.1 \pm {}^{1.9}_{1.1}$ (1.5–7.3)	Adopted $P = 0.060$	

Table 1 – *continued*

Object	$z_{\rm phot}^{\rm CY}$	$z_{\rm phot}^{\rm A}$	Notes	$z_{\rm spec}$
SHADES J105235+572514 (Lock850.47)	$\geqslant$2.0	$\geqslant$1.5		
SHADES J105256+573245 (Lock850.48)	$3.1 \pm {}^{1.1}_{0.6}$	$2.4 \pm {}^{1.6}_{0.9}$ (1.2–6.2)	Adopted $P = 0.068$	
SHADES J105245+573121 (Lock850.52)	$3.1 \pm {}^{2.0}_{1.4}$	$2.6 \pm {}^{1.6}_{1.1}$ (0.5–5.7)		
SHADES J105240+571928 (Lock850.53)	$\geqslant$2.3	$\geqslant$1.5		
SHADES J105143+572446 (Lock850.60)	$\geqslant$1.4	$\geqslant$0.8		
SHADES J105153+572505 (Lock850.63)	$3.9 \pm {}^{2.6}_{1.7}$	$2.6 \pm {}^{2.0}_{0.6}$ (1.5–6.7)		
SHADES J105251+573242 (Lock850.64)	$\geqslant$2.3	$\geqslant$1.5		
SHADES J105138+572017 (Lock850.66)	$\geqslant$2.6	$\geqslant$2.0		
SHADES J105209+572355 (Lock850.67)	$\geqslant$1.7	$\geqslant$1.0		
SHADES J105148+573046 (Lock850.70)	$\geqslant$1.9	$\geqslant$1.5		
SHADES J105218+571903 (Lock850.71)	$2.1 \pm {}^{1.1}_{0.8}$	$1.6 \pm {}^{1.1}_{0.6}$ (0.8–4.2)		
SHADES J105141+572217 (Lock850.73)	$3.5 \pm {}^{2.3}_{1.7}$	$2.6 \pm {}^{1.1}_{0.6}$ (1.0–6.2)	N	
	$2.5 \pm {}^{1.5}_{1.0}$	$2.1 \pm {}^{1.1}_{1.1}$ (0.5–5.0)	Co-added	
SHADES J105315+572645 (Lock850.75)	$\geqslant$1.2	$\geqslant$1.1		
SHADES J105148+572838 (Lock850.76)	$3.0 \pm {}^{1.8}_{1.3}$	$2.1 \pm {}^{1.9}_{0.9}$ (0.8–6.0)		
SHADES J105157+572210 (Lock850.77)	$4.5 \pm {}^{3.1}_{2.4}$	$3.1 \pm {}^{1.0}_{0.6}$ (1.5–7.0)	S	
	$2.4 \pm {}^{0.4}_{0.5}$	$1.9 \pm {}^{1.1}_{0.8}$ (0.8–4.8)	S+N	
SHADES J105145+571738 (Lock850.78)	$\geqslant$1.9	$\geqslant$1.3		
SHADES J105152+572127 (Lock850.79)	$3.6 \pm {}^{2.4}_{1.6}$	$2.6 \pm {}^{2.0}_{0.6}$ (1.2–6.5)	Adopted $P = 0.064$	
SHADES J105231+571800 (Lock850.81)	$\geqslant$2.2	$\geqslant$1.9		
SHADES J105307+572839 (Lock850.83)	$\geqslant$2.1	$\geqslant$0.8		
SHADES J105153+571733 (Lock850.87)	$2.1 \pm {}^{1.1}_{0.8}$	$1.6 \pm {}^{1.1}_{0.6}$ (0.5–4.2)		
SHADES J105139+571509 (Lock850.100)	$\geqslant$4.0	$\geqslant$3.0		

[a]This source has a robust 1.4 GHz association in the data set of Ivison et al. (2002), but it is below the robustness level adopted for the analysis in this paper, and thus we will make use of the revised 1.4 GHz photometry of Ivison et al. (2007) as an upper limit.

2.1.3 Redshift distribution of the SHADES population

We have assembled the best estimates of photometric redshift for each source in the LH and SXDF SHADES fields (Fig. 3). These are identified by the modes of the individual probability distributions, $z_{\rm phot}^{\rm A}$, which, by definition, are the redshifts with the highest probability values.

The galaxies that are not detected with confidence at radio wavelengths, i.e. 26 out of the 60 galaxies in the LH, and 25 out of the 60 in the SXDF, have very flat individual redshift probability distributions in our computations, and hence we quote only the lower limits to their redshift, which are defined as their 90 per cent lower confidence limits (Tables 1 and 2). We incorporate these objects into the population distribution by adding flat probability distributions between their calculated lower 90 per cent confidence limits and $z = 5$, and alternatively between their calculated lower 90 per cent confidence limits and $z = 2$, or only at their lower redshift limits if these indicate $z > 2$. These two alternative priors illustrate how the resulting redshift distributions (that include SHADES galaxies without radio detections) can be biased high and low.

Fig. 3 shows the final photometric-redshift distribution using the 1.4 GHz/850 μm spectral index, both for the full SHADES sample and for the LH and SXDF fields separately. The redshift distribution of SXDF sources peaks at slightly lower redshifts (median $z \approx 2.2$) compared to the distribution of LH sources (median $z \approx 2.6$). The low-redshift tail ($z < 1.5$) is also slightly more prominent in the SXDF than in the LH (six versus one sources among the radio-detected sample). The difference in shape of the two distributions of radio-detected sources can be measured using the two-tailed Kolmogorov–Smirnov (KS) test, which gives a 3 per cent chance that they are drawn from the same parent distribution. Furthermore, the mean redshifts of the two distributions are significantly different at the 99.7 per cent level, according to a Mann–Whitney *U*-test. This difference can be attributed to differences in the noise levels of the radio maps, although some intrinsic variations between the fields are expected (see Section 3).

For those objects with more than one redshift estimate (due to the ambiguity in their counterparts), we have produced alternative population distributions, with or without their inclusion, and with different combinations of possible counterparts. The results do not significantly change the final combined distribution. All figures presented in this paper include the primary radio association if there are multiple options.

2.2 Radio–mm–FIR SED analysis

The SHADES fields have been targeted by other FIR/sub-mm/mm and radio surveys. In this section, we describe the extra constraints on the photometric redshifts that can be derived from these additional complementary data for a few tens of SHADES sources.

2.2.1 Techniques and accuracies

Photometric redshifts with modest precisions ($\Delta z \approx 0.3$ to 0.5) have been obtained in the past few years using a combination of spectral indices between the radio and mm-wavelength regimes and the FIR spectral peak. This information has been exploited by several groups using a wide array of fitting techniques and

Table 2. Same as Table 1 for SHADES sources in the SXDF field.

Object	z^{CY}_{phot}	z^{A}_{phot}	Notes	z_{spec}
SHADES J021730−045937 (SXDF850.1)	$4.3 \pm ^{2.9}_{1.7}$	$3.1 \pm ^{2.0}_{0.6}$ (2.0–6.8)		
SHADES J021803−045527 (SXDF850.2)	$2.6 \pm ^{1.4}_{1.0}$	$2.6 \pm ^{0.7}_{1.1}$ (1.2–5.1)		
SHADES J021742−045628 (SXDF850.3)	$3.3 \pm ^{1.8}_{1.3}$	$2.1 \pm ^{1.8}_{0.4}$ (1.5–6.0)		
SHADES J021738−050337 (SXDF850.4)	$1.7 \pm ^{0.9}_{0.6}$	$1.1 \pm ^{1.1}_{0.3}$ (0.5–3.5)		
SHADES J021802−050032 (SXDF850.5)	$1.4 \pm ^{0.6}_{0.5}$	$1.1 \pm ^{0.6}_{0.5}$ (0.5–2.8)		
SHADES J021729−050326 (SXDF850.6)	$3.1 \pm ^{0.6}_{0.5}$	$2.4 \pm ^{1.9}_{0.6}$ (1.3–6.0)	NW	
	$3.6 \pm ^{1.1}_{1.5}$	$2.9 \pm ^{1.6}_{1.1}$ (1.6–6.5)	N	
SHADES J021738−050523 (SXDF850.7)	$4.1 \pm ^{2.8}_{1.7}$	$2.6 \pm ^{1.9}_{0.6}$ (2.0–7.2)		
SHADES J021744−045554 (SXDF850.8)	$3.3 \pm ^{1.9}_{1.3}$	$2.6 \pm ^{1.6}_{0.7}$ (1.2–5.9)		
SHADES J021756−045806 (SXDF850.9)	$\geqslant$2.1	$\geqslant$1.6		
SHADES J021825−045557 (SXDF850.10)	$2.3 \pm ^{1.3}_{0.8}$	$1.6 \pm ^{1.4}_{0.4}$ (1.0–4.8)		
SHADES J021725−045937 (SXDF850.11)	$2.8 \pm ^{1.5}_{1.2}$	$2.1 \pm ^{1.6}_{0.6}$ (1.0–5.6)		
SHADES J021759−050503 (SXDF850.12)	$3.6 \pm ^{2.2}_{1.5}$	$2.6 \pm ^{1.7}_{0.9}$ (1.5–6.7)		
SHADES J021819−050244 (SXDF850.14)	$3.4 \pm ^{2.0}_{1.6}$	$2.6 \pm ^{1.6}_{1.0}$ (1.2–6.5)		
SHADES J021815−045405 (SXDF850.15)	$\geqslant$2.5	$\geqslant$2.0		
SHADES J021813−045741 (SXDF850.16)	$3.5 \pm ^{2.1}_{1.6}$	$2.6 \pm ^{1.9}_{0.6}$ (1.5–6.5)		
SHADES J021754−045302 (SXDF850.17)	$\geqslant$2.7	$\geqslant$2.2		
SHADES J021757−050029 (SXDF850.18)	$3.9 \pm ^{2.5}_{1.7}$	$2.6 \pm ^{2.0}_{0.6}$ (1.5–6.5)		
SHADES J021828−045839 (SXDF850.19)	$2.2 \pm ^{1.2}_{0.8}$	$1.6 \pm ^{1.1}_{0.6}$ (0.8–4.6)		
SHADES J021744−050216 (SXDF850.20)	$\geqslant$1.7	$\geqslant$1.4		
SHADES J021742−050427 (SXDF850.21)	$0.9 \pm ^{0.6}_{0.4}$	$0.6 \pm ^{0.9}_{0.2}$ (0.0–2.2)		
SHADES J021800−050741 (SXDF850.22)	$\geqslant$1.7	$\geqslant$1.8		
SHADES J021742−050545 (SXDF850.23)	$2.7 \pm ^{1.5}_{1.0}$	$2.1 \pm ^{1.4}_{0.6}$ (1.0–5.0)		
SHADES J021734−050437 (SXDF850.24)	$3.4 \pm ^{2.0}_{1.7}$	$2.1 \pm ^{1.8}_{0.6}$ (1.0–6.1)	N	
	$3.7 \pm ^{2.4}_{1.8}$	$2.6 \pm ^{2.0}_{0.6}$ (1.5–7.0)	S	
SHADES J021812−050555 (SXDF850.25)	$\geqslant$1.6	$\geqslant$1.0		
SHADES J021807−050148 (SXDF850.27)	$1.5 \pm ^{0.8}_{0.6}$	$1.1 \pm ^{0.9}_{0.5}$ (0.5–3.3)		
SHADES J021807−045915 (SXDF850.28)	$2.3 \pm ^{1.3}_{0.9}$	$1.6 \pm ^{1.4}_{0.6}$ (0.5–4.5)	N	
	$1.7 \pm ^{1.0}_{0.6}$	$1.1 \pm ^{1.1}_{0.3}$ (0.2–3.5)	N+S	
SHADES J021816−045511 (SXDF850.29)	$1.6 \pm ^{0.9}_{0.6}$	$1.1 \pm ^{0.9}_{0.4}$ (0.6–3.5)		
SHADES J021740−050116 (SXDF850.30)	$4.4 \pm ^{3.1}_{2.0}$	$3.1 \pm ^{1.7}_{1.1}$ (1.8–7.7)		
SHADES J021736−045557 (SXDF850.31)	$3.2 \pm ^{1.8}_{1.3}$	$2.1 \pm ^{1.6}_{0.6}$ (1.5–6.2)		
SHADES J021722−050038 (SXDF850.32)	$\geqslant$2.1	$\geqslant$1.5		
SHADES J021800−045311 (SXDF850.35)	$3.3 \pm ^{2.0}_{1.5}$	$2.1 \pm ^{2.1}_{0.5}$ (1.0–6.1)		
SHADES J021832−045947 (SXDF850.36)	$\geqslant$1.9	$\geqslant$1.8		
SHADES J021724−045839 (SXDF850.37)	$3.2 \pm ^{2.0}_{1.5}$	$2.1 \pm ^{2.1}_{0.5}$ (0.8–6.1)		
SHADES J021825−045714 (SXDF850.38)	$2.7 \pm ^{1.6}_{1.3}$	$2.1 \pm ^{1.6}_{0.8}$ (0.5–5.4)		
SHADES J021750−045540 (SXDF850.39)	$\geqslant$1.7	$\geqslant$1.5		
SHADES J021729−050059 (SXDF850.40)	$2.9 \pm ^{1.6}_{1.4}$	$2.1 \pm ^{2.0}_{0.6}$ (1.0–5.9)		
SHADES J021829−050540 (SXDF850.45)	$\geqslant$4.4	$\geqslant$3.3		
SHADES J021733−045857 (SXDF850.47)	$1.5 \pm ^{0.9}_{0.6}$	$1.1 \pm ^{0.8}_{0.6}$ (0.2–3.1)	NE	
	$2.6 \pm ^{1.6}_{1.1}$	$2.1 \pm ^{1.4}_{1.0}$ (0.6–5.2)	SE	
	$1.3 \pm ^{0.7}_{0.5}$	$1.1 \pm ^{0.7}_{0.6}$ (0.2–2.9)	NE+SE	
	$2.2 \pm ^{1.2}_{1.0}$	$1.6 \pm ^{1.3}_{0.6}$ (0.5–4.4)	W	
SHADES J021724−045717 (SXDF850.48)	$\geqslant$2.6	$\geqslant$1.8		
SHADES J021820−045648 (SXDF850.49)	$\geqslant$1.3	$\geqslant$1.0		
SHADES J021802−045645 (SXDF850.50)	$3.6 \pm ^{2.3}_{1.7}$	$2.1 \pm ^{2.1}_{0.6}$ (1.2–6.9)		
SHADES J021804−050453 (SXDF850.52)	$2.0 \pm ^{1.1}_{0.8}$	$1.6 \pm ^{1.1}_{0.6}$ (0.5–4.1)	E	
	$1.5 \pm ^{0.9}_{0.6}$	$1.1 \pm ^{0.9}_{0.6}$ (0.2–3.1)	ES	

Table 2 – *continued*

Object	$z_{\rm phot}^{\rm CY}$	$z_{\rm phot}^{\rm A}$	Notes	$z_{\rm spec}$
SHADES J021752−050446 (SXDF850.55)	$3.0 \pm {}^{1.7}_{1.6}$	$2.1 \pm {}^{2.1}_{0.6}$ (0.8–6.1)		
SHADES J021750−050631 (SXDF850.56)	$\geqslant$1.2	$\geqslant$0.6		
SHADES J021745−045750 (SXDF850.63)	$\geqslant$1.6	$\geqslant$1.5		
SHADES J021807−050403 (SXDF850.65)	$\geqslant$2.2	$\geqslant$1.2		
SHADES J021751−050250 (SXDF850.69)	$\geqslant$1.5	$\geqslant$1.0		
SHADES J021811−050247 (SXDF850.70)	$\geqslant$1.9	$\geqslant$1.2		
SHADES J021821−045903 (SXDF850.71)	$\geqslant$1.7	$\geqslant$1.2		
SHADES J021758−045428 (SXDF850.74)	$2.9 \pm {}^{1.7}_{1.5}$	$2.1 \pm {}^{1.6}_{1.1}$ (0.8–5.8)		
SHADES J021755−050621 (SXDF850.76)	$\geqslant$1.9	$\geqslant$1.5		
SHADES J021736−050432 (SXDF850.77)	$2.9 \pm {}^{1.7}_{1.5}$	$2.1 \pm {}^{2.1}_{0.6}$ (1.0–6.1)		
SHADES J021817−050404 (SXDF850.86)	$\geqslant$1.5	$\geqslant$1.0		
SHADES J021800−050448 (SXDF850.88)	$\geqslant$1.0	$\geqslant$1.0		
SHADES J021734−045723 (SXDF850.91)	$\geqslant$1.5	$\geqslant$1.2		
SHADES J021733−045813 (SXDF850.93)	$\geqslant$1.9	$\geqslant$0.8		
SHADES J021740−045817 (SXDF850.94)	$\geqslant$1.5	$\geqslant$1.2		
SHADES J021741−045833 (SXDF850.95)	$\geqslant$1.6	$\geqslant$1.0		
SHADES J021800−050212 (SXDF850.96)	$3.5 \pm {}^{2.1}_{1.6}$	$3.1 \pm {}^{1.1}_{1.5}$ (1.0–6.3)		
SHADES J021756−045255 (SXDF850.119)	$3.4 \pm {}^{2.0}_{1.6}$	$2.6 \pm {}^{1.7}_{1.1}$ (0.8–6.2)		

SEDs (e.g. Hughes et al. 2002; Yun & Carilli 2002; Aretxaga et al. 2003; Wiklind 2003; Aretxaga et al. 2005; Hunt & Maiolino 2005; Laurent et al. 2006). There remain, however, degeneracies imposed by the choice of multiple SED templates, with FIR emission peaks distributed over a range of wavelengths, which can limit the precision of the derived redshifts (e.g. Blain, Barnard & Chapman 2003). We have previously developed a radio–mm–FIR technique based on Monte Carlo (MC) simulations that take into account constraining prior information such as the number counts of sub-mm galaxies, the favoured luminosity/density evolution up to $z \approx 2$ and the lensing amplification of a certain field (Hughes et al. 2002; Aretxaga et al. 2003, 2005). We only offer a brief summary of this technique here. A catalogue of 60 μm luminosities and redshifts for mock galaxies is generated from an evolutionary model for the 60 μm luminosity function that fits the observed 850 μm number counts [e.g. luminosity evolution $\propto (1+z)^3$ for $z \lesssim 2$, and no evolution at $z > 2$] and covers a simulated area of 10 deg^2. Template SEDs are drawn at random, without regard to their intrinsic luminosity, from a library of 20 local starbursts, ULIRGs and AGN, to provide FIR–radio colours for the mock galaxies. The SEDs cover a wide range of FIR luminosities ($9.0 < \log L_{\rm FIR}/{\rm L}_\odot < 12.3$) and temperatures ($25 < T/K < 65$). The flux densities of the mock galaxies include both photometric and calibration errors, consistent with the quality of the observational data for each sub-mm galaxy detected in a particular survey. We reject from the catalogue those mock galaxies that do not respect the detection thresholds and upper limits of the particular sub-mm galaxy under analysis. The redshift probability distribution of an individual sub-mm galaxy is then calculated as the normalized distribution of the redshifts of the mock galaxies in the reduced catalogue, weighted by the likelihood of identifying the colours and flux densities of each mock galaxy with those of the sub-mm galaxy in question. This technique will be denoted by $z_{\rm phot}^{\rm MC}$ in the discussion that follows.

The validity of the results derived from this technique is limited by the assumption that the SEDs of high-redshift sub-mm galaxies are similar to the local analogues, adopted as templates, which are scaled in luminosity and shifted in redshift. While this might seem a naive approach, all the templates used in the calculations that follow offer a good description of the radio–mm–FIR photometry of SCUBA galaxies, including 350 μm observations (Kovács et al. 2006; Laurent et al. 2006), with known spectroscopic redshifts and unambiguous multiwavelength counterparts (Aretxaga et al. 2005). There are, however, a few sub-mm galaxies which do not match any of the templates we use in this paper at their published redshifts (see fig. 4 in Aretxaga et al. 2006). In these examples, their radio emission is higher than that implied by the radio–FIR correlation, possibly due to accretion activity, or their FIR emission peaks at wavelengths longer than those of the templates used in this study at the adopted redshift. We describe the redshift solutions for these galaxies as 'catastrophic' and this might be indicative of incompleteness in the library of SED templates used as analogues. There is still sufficient debate in the literature, however, about the nature and/or the ambiguity of the multiwavelength counterparts to these sub-mm sources from which the redshifts are derived to justify their exclusion from a robust comparison sample (see Aretxaga et al. 2005, 2006; Kovács et al. 2006; Laurent et al. 2006, for a detailed complementary discussion on these galaxies).

In order to estimate the accuracy of the $z_{\rm phot}^{\rm MC}$ technique, we use the full SED information of a robust sub-sample of 11 sub-mm galaxies, out of the comparison sample of 58 galaxies considered in Section 2.1.1, which have detections in three or more bands. Furthermore, the same galaxies have undisputed identifications of their optical/IR/radio counterparts and spectroscopic redshifts derived from the measurement of two or more spectral lines. We derive a mean accuracy for this sub-sample of $\Delta z \equiv \langle\, |z_{\rm phot}^{\rm MC} - z_{\rm spec}|\,\rangle \approx 0.2$ and a rms $\langle\, (z_{\rm phot}^{\rm MC} - z_{\rm spec})^2\,\rangle^{1/2} \approx 0.25$ over the whole redshift interval (Fig. 4). Using all objects with published photometry, regardless of whether the spectroscopic redshift derived from the optical associations is ambiguous or not, the overall accuracy over the $0 \leqslant z \leqslant 4$ regime degrades to $\Delta z \approx 0.55$, with a rms of 0.80 (see fig. 3 in Aretxaga et al. 2006). A few significant outliers which remain in the correlation are discussed by Aretxaga et al. (2005) and Kovács et al. (2006). Within the small sub-sample of study, the accuracy is independent of redshift.

If we restrict the use of photometry to 450 μm upper limits combined with the 1.4 GHz and 850 μm detections for the comparison sample of galaxies (adopting simulated 450 μm upper limits, when necessary, to mimic a shallower survey at this wavelength), we find

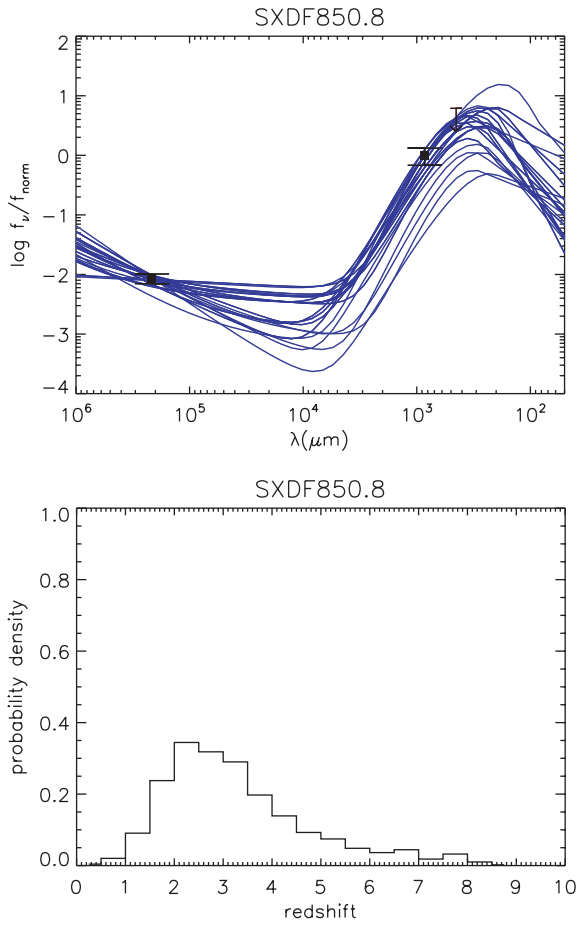

Figure 2. Top: SED of SXDF850.8, where the black squares mark the detections at 850 μm and 1.4 GHz used in the photometric-redshift calculation. Error bars are 1σ, and the arrow at 450 μm marks the 3σ upper limit derived from our maps. For reference, the SED templates used in the photometric-redshift calculation are shifted to $z^{A}_{phot} = 2.6$ and scaled to maximize the likelihood function of detections and upper limit through survival analysis (Isobe et al. 1986), and are represented as lines. All the SEDs are compatible within the 3σ error bars of the photometry of the source. Bottom: probability distribution for SXDF850.8 derived for the z^{A}_{phot} solution, using only the 850 μm and 1.4 GHz photometry.

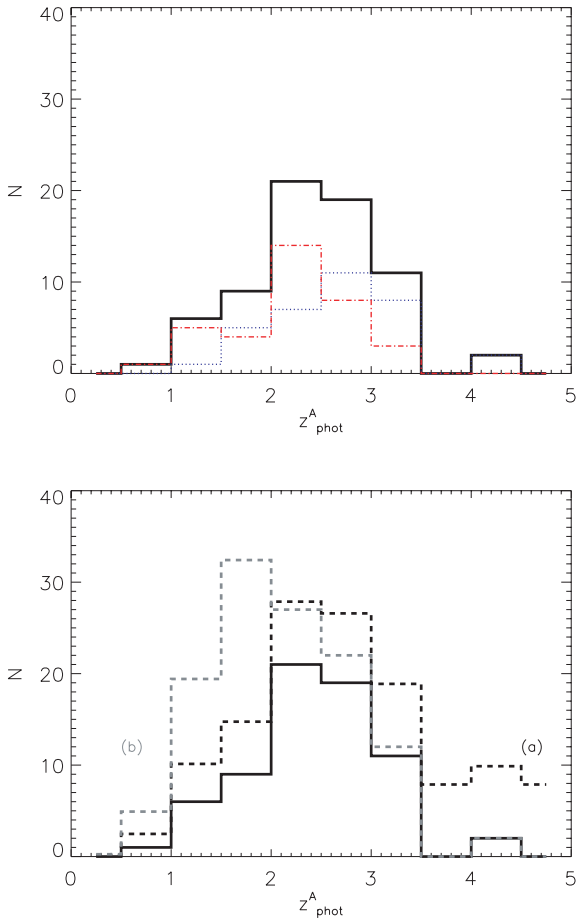

Figure 3. Histogram of modes of the photometric-redshift distributions of SHADES galaxies derived from the 1.4 GHz/850 μm spectral index. The (black) thick solid line (shown in the upper and lower panels) represents the distribution of modes for the 69 galaxies that have been detected at both 850 μm and 1.4 GHz. In the upper panel, the (blue) thin dotted line and (red) thin dash–dotted line represent the redshift distributions in the LH and SXDF fields, respectively. In the lower panel, the black dashed line (a) and grey dashed line (b) show the redshift distributions for the full SHADES catalogue, including the 51 sub-mm galaxies undetected at 1.4 GHz. Those SCUBA galaxies with non-detections in the radio are distributed in one of two ways that bracket the range of reasonable options: (a) with equal probability between their calculated lower 90 per cent confidence limits and $z = 5$; and alternatively, (b) between their lower limits and $z = 2$, or only at their lower redshift limits in the cases that these lie at $z > 2$.

a mean accuracy of $\Delta z \approx 0.55$ and a rms of 0.7 for the robust sample. This result is especially relevant for the photometric-redshift calculations of the SHADES sources in Section 2.2.2, the majority of which have similarly sparsely sampled photometry. Considering only the complete sample with robust and tentative spectroscopic redshifts, the mean accuracy degrades slightly to $\Delta z \approx 0.65$, and the rms scatter is 0.90.

2.2.2 The redshifts of SHADES sources

Table 3 summarizes the most recent photometric redshifts calculated with the MC technique for SHADES sources with additional photometry published in the literature. In contrast, and for completeness, Tables 4 and 5 list the photometric redshifts derived only from the combination of the SHADES 450/850 μm and the 1.4 GHz photometry using two approaches: the MC based technique, z^{MC}_{phot}, described above, and a non-prior maximum-likelihood fit to the same 20 SEDs used for the first method that includes survival analysis (Isobe, Feigelson & Nelson 1986) to incorporate the non-detections into the maximum-likelihood formalism, z^{SA}_{phot}. This second technique is introduced to provide a comparison of how the priors affect the redshift estimation of the sources and the final combined redshift distribution of SHADES galaxies. While most of the photometric redshifts derived from the two methods are similar, the pure survival analysis produces a few high-redshift catastrophic results in the robust comparison sample (two out of 11). The overall reliability of the maximum-likelihood technique is $\Delta z \approx 0.7$. These high-redshift catastrophic solutions get suppressed by the MC technique due to the weighting priors that disfavour high- redshift solutions for these sources, since, if they were typical of the sub-mm population, they would overproduce the 850 μm number counts under the assumed luminosity evolution model. Although we give the values of photometric redshifts with and without priors in Tables 4 and 5, we will now continue the analysis of the complete SHADES sample using

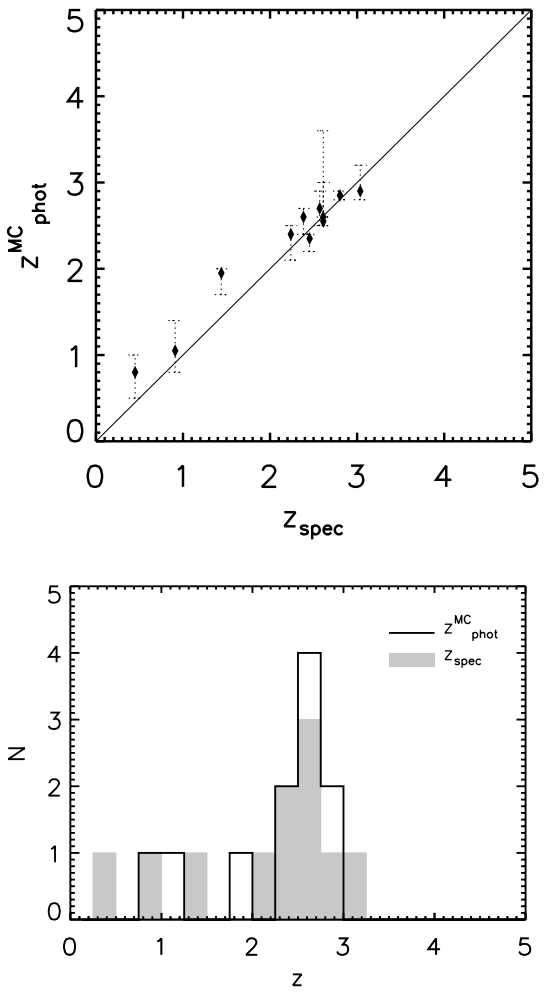

Figure 4. Top: comparison of spectroscopic and photometric redshifts derived from the full radio–FIR SED for a sample of 11 sub-mm galaxies with at least three robust detections at different wavelengths. This sample has undisputed radio/optical/IR counterparts associated with the sub-mm galaxies, and spectroscopic redshifts derived from two or more lines. The relationship has a rms of 0.25. Bottom: comparison of the distributions of the spectroscopic and photometric redshifts represented in the top panel.

only the MC solutions, since they have been shown to perform better against the comparison sample.

For five sources in Table 5, SXDF850.5, 21, 28, 77 and 119, we also include complementary photometry at 70 and 160 μm from the *Spitzer* Legacy Survey SWIRE (Lonsdale et al. 2003; Surace et al., in preparation) that are used to derive mid-IR counterparts to the SHADES sources (Clements et al., in preparation). The remainder of the SHADES sources are not significantly detected ($\geqslant 4\sigma$) in the *Spitzer* catalogues, and the noise properties of the SWIRE maps, providing 3σ upper limits of ∼23 and 160 mJy at 70 and 160 μm, respectively (Afonso-Luis et al., in preparation), do not further constrain the photometric redshifts.

Fig. 5 shows the single-peaked redshift probability distribution derived for one of the sources that have the most complete photometric data. Although the majority of the sources show similar probability distributions, there are sometimes secondary peaks (see examples in Aretxaga et al. 2003). Nevertheless, it is always the primary redshift peak that defines the solutions given in Tables 3–5.

2.2.3 *Redshift distribution of the SHADES population*

Fig. 6 shows our final photometrically derived redshift distribution for the SHADES sources, using our best available estimate for the redshift of each source (i.e. $z_{\rm phot}^{\rm MC}$ taken from Table 3 for those sources with the most complete photometry, and from Tables 4 and 5 for the remainder).

The distribution of radio-identified SHADES sources clearly peaks in the bin $z \approx 2.0$–2.5, with a 50 per cent interquartile interval $z \sim 1.8$–3.1. We incorporate the non-radio detected sources (lower panel in Fig. 6) into the population distribution in two alternative ways to serve as examples of how much these sources could alter the final population distribution: (a) approximating their individual probability distributions as flat distributions between their lower 90 per cent confidence limit and $z = 5$ and (b) as flat distributions between their lower 90 per cent confidence limit and $z = 2$, or at their lower limit if this lies at $z > 2$. Solution (a) is actually derived from the adopted non-informative (flat) prior for the photometric-redshift calculations. This creates a high-redshift tail which is a reflection of the adopted range for the flat redshift distributions which are unconstrained by the photometry. Solution (b) is biased against high redshift by imposing a maximum redshift for the radio-undetected sample which is lower than the redshift of the peak of the radio-detected sample. This radio-undetected sample could be composed of colder sub-mm galaxies than those found in the template library, or they could have the same template shapes as those adopted in the photometric-redshift analysis, and still be undetected at the depth of the present radio surveys. Regardless, in these alternative solutions, the mode of the population remains at $z \approx 2.0$–2.5, with at least 50 per cent of the galaxies in the interquartile range $1.6 \leqslant z \leqslant 3.4$.

In order to consider the effect of the objects with more than one redshift estimate (due to ambiguity in their radio counterparts), we have produced alternative population distributions. For instance, Fig. 6 shows the combination of the first entries for each source in Tables 3–5. The introduction of the second tabulated values instead of the first ones, for those sources with ambiguous associated photometry, produces an alternative distribution which is indistinguishable (with a 99.96 per cent probability), via a KS test, from the one represented here.

As in the case of the photometric-redshift distribution derived from the 1.4 GHz/850 μm spectral index, the distribution of redshifts derived from the full SED analysis of SXDF sources peaks at slightly lower redshifts (median $z \approx 2.2$) than that of LH sources (median $z \approx 2.7$), and its low-redshift tail ($z < 1.5$) is also more prominent. These differences in the distributions are statistically significant, as indicated by a KS test at a level of 98.9 per cent. A Mann–Whitney *U*-test shows that their mean redshifts differ at the 99.997 per cent level.

3 DISCUSSION

3.1 Redshift distribution

SHADES was designed with the objective of constraining the redshift distribution and clustering properties of the sub-mm galaxy population, an exercise which van Kampen et al. (2005) demonstrated could discriminate between galaxy formation models. With ∼40 per cent of the survey completed before SCUBA was decommissioned in the summer 2005, SHADES has provided 120 robust sources. The radio–mm–FIR photometry assembled for the survey favours a nearly Gaussian redshift distribution of the

Table 3. Photometric redshifts for the sources with additional radio–mm–FIR data reported in the literature from other surveys. The photometry has been complemented at other wavelengths, while preserving the SHADES 450/850 μm (Coppin et al. 2006) and 1.4 GHz (Ivison et al. 2007) determined flux densities. The first column gives the source name; the second column gives the most probable mode and error bars based on the 68 per cent confidence interval of the mode calculation (in parenthesis the 90 per cent confidence interval); the third and fourth columns, respectively, give the bands in which the source is detected at a $\geqslant 3\sigma$ level, and at which upper limits are used for the computation of the photometric redshifts; the fifth column provides the published references (and alternative source names in overlapping surveys) to the additional photometry, using the following syntax: LE850.x from Scott et al. (2002), 1100.x from Laurent et al. (2005, 2006) and 1200.x from Greve et al. (2004) and Ivison et al. (2005).

Object	$z_{\rm phot}$	$\geqslant 3\sigma$ detections	$<3\sigma$/upper limits	Notes
Lock850.1	$2.4 \pm {}^{1.1}_{0.2}$ (2.2–3.8)	350, 850 μm, 1.1, 1.2 mm, 1.4 GHz	175, 450 μm, 3.3 mm, 5 GHz	LE850.1, 1200.5, 1100.14
Lock850.2	$2.9 \pm {}^{0.3}_{0.1}$ (2.5–3.8)	350, 850 μm, 1.1, 1.2 mm, 1.4 GHz	450 μm	LE1100.1, 1200.4, SW-1.4 GHz
	$2.9 \pm {}^{0.7}_{0.1}$ (2.8–3.9)			NW-1.4 GHz
Lock850.3	$2.9 \pm {}^{0.9}_{0.3}$ (2.5–4.2)	350, 850 μm, 1.1, 1.2 mm, 1.4 GHz	450 μm, 5 GHz	LE850.2, 1100.8, 1200.1, S-1.4 GHz
	$2.6 \pm {}^{0.3}_{0.1}$ (2.5–3.8)			Co-added-1.4 GHz
Lock850.4	$1.6 \pm {}^{0.3}_{0.1}$ (1.5–4.8)	850 μm, 1.2 mm, 1.4 GHz	450 μm, 5 GHz	LE850.14, 1200.3
Lock850.12	$2.6 \pm {}^{0.2}_{0.1}$ (2.2–3.0)	350, 850 μm, 1.1, 1.2 mm, 1.4 GHz	450 μm, 5 GHz	LE850.16, 1100.16, 1200.6
Lock850.14	$2.6 \pm {}^{0.8}_{0.1}$ (2.2–3.7)	350, 850 μm, 1.1, 1.2 mm	450 μm, 1.4, 5 GHz	LE850.6, 1100.5, 1200.10[a]
Lock850.16	$1.9 \pm {}^{0.4}_{0.1}$ (1.5–3.2)	850 μm, 1.2 mm,1.4 GHz	450 μm, 5 GHz	LE850.7
Lock850.17	$2.5 \pm {}^{0.6}_{0.5}$ (2.0–5.9)	850 μm, 1.2 mm, 5, 1.4 GHz	450 μm	LE850.3, 1200.11
Lock850.18	$3.1 \pm {}^{2.9}_{0.1}$ (2.3–6.0)	850 μm, 1.2 mm, 1.4 GHz	450 μm	LE1200.9
Lock850.27	$4.6 \pm {}^{1.4}_{0.4}$ (4.0–6.0)	850 μm, 1.1, 1.2 mm, 1.4 GHz	450 μm, 5 GHz	LE1100.4, 1200.7
Lock850.33	$3.6 \pm {}^{0.7}_{0.9}$ (2.4–4.8)	850 μm, 1.2 mm, 1.4 GHz	450 μm	LE850.18, 1200.12
Lock850.41	$3.4 \pm {}^{0.7}_{0.2}$ (3.2–4.4)	350, 850 μm, 1.1, 1.2 mm, 1.4 GHz	450 μm	LE850.8, 1100.17, 1200.14
Lock850.76	$4.6 \pm {}^{1.4}_{1.1}$ (3.0–6.0)	850 μm, 1.1 mm, 1.4 GHz	450 μm	LE1100.15

[a]This source has a robust 1.4 GHz association in the data set of Ivison et al. (2002), but it is below the robustness level adopted for the analysis in this paper, and thus we will make use of the 1.4 GHz photometry of Ivison et al. (2007) as an upper limit.

population peaking at $z \approx 2.0$–2.5, albeit still with the possibility of a high-redshift tail remaining.

The photometric-redshift distribution of the radio-detected sub-mm galaxies is qualitatively similar to the optical spectroscopic redshift distribution published by Chapman et al. (2003, 2005) who followed-up a sample of sub-mm galaxies derived from various surveys. The agreement is perhaps not surprising, given that the photometric redshifts of the comparison sample have shown a relatively good agreement with the spectroscopic redshifts published in the literature (Aretxaga et al. 2006, Sections 2.1.1 and 2.2.1). Furthermore, the majority of the sub-mm sources that have spectroscopic redshifts are drawn from SCUBA surveys of similar depths to SHADES.

The high-redshift correction applied to the measured spectroscopic redshift distribution, suggested by Chapman et al. (2005) to account for the bias introduced by non-detection of the higher-redshift radio counterparts that provide candidates for optical spectroscopic follow-up, also falls within the range of photometric-redshift estimations we have derived for SHADES sources that are not detected at radio wavelengths. These sources provide the high-redshift ($z > 3$) tail of Fig. 6, and could in fact be placed anywhere above $z \sim 1.0$, even producing secondary peaks.

Our calculations do not support the existence of a substantial low-redshift ($z < 1.5$) tail within the luminous sub-mm radio-detected population sampled by SHADES. At first sight, this might appear to be in conflict with the results of Pope et al. (2005, 2006) who found that ∼30 per cent of the sub-mm sources found in the SCUBA imaging of the GOODS-North field may lie at $z < 1.5$. If the GOODS-North 850 μm catalogue is restricted to sources with de-boosted flux densities $S_{850} > 3$ mJy, however, then the proportion of robustly identified sub-mm galaxies which lie at $z < 1.5$ drops to 6 per cent. This is entirely consistent with the results found here for SHADES galaxies. Thus, these results may be providing further evidence that the peak of the redshift distribution of sub-mm sources is positively correlated with sub-mm flux-density/luminosity, consistent with the apparently anti-hierarchical nature of star formation history reported in several other recent studies (e.g. Heavens et al. 2004). Furthermore, field-to-field variations in the spatial distribution of the large-scale structure can provide a simple explanation for the differences between the redshift distributions of sub-mm sources derived from the individually mapped contiguous areas (typically < 0.2 deg^2) taken from the current generation of SCUBA surveys.

Our analysis also suggests that only a modest fraction of sub-mm galaxies could be hiding in the optical redshift desert at $z \approx 1.5$–1.8 during spectroscopic searches for SHADES sources with robust radio counterparts. The photometric-redshift probability density distributions of radio-detected SHADES sources using the 1.4 GHz/850 μm index or the full radio–mm–FIR SED information contain ∼15 and ∼10 per cent of sources in this redshift desert regime, respectively.

The difference between the redshift distribution of sub-mm sources in the SXDF and LH fields is entirely consistent with the different properties of the 1.4-GHz maps as discussed by Ivison et al. (2007). The LH data have a higher VLA resolution than those in SXDF, and the LH data are also deeper, although the coverage is less uniform. There is clearly potential for systematic differences between radio measurements in the LH and SXDF. For an extended source in the LH (of which there are several – Ivison et al. 2002), a larger fraction of emission on scales larger than the synthesized beam will be resolved away than for similar cases in SXDF. Moreover, the LH data will suffer greater significant bandwidth smearing and, although the appropriate correction has been made to the

Table 4. Photometric redshifts for SHADES sources in the LH field based on the 850 μm and 1.4 GHz data and 450 μm upper limits determined by SHADES. The columns give (1) name of the source; (2) $z_{\rm phot}^{\rm SA}$ survival analysis solution; (3) $z_{\rm phot}^{\rm MC}$ MC solution and (4) notes on associations.

Object	$z_{\rm phot}^{\rm SA}$	$z_{\rm phot}^{\rm MC}$	Notes
Lock850.1	$2.1 \pm {}^{2.0}_{0.1}$ (1.5–5.9)	$2.4 \pm {}^{0.1}_{0.2}$ (2.0–2.5)	
Lock850.2	$3.1 \pm {}^{2.8}_{0.1}$ (2.4–6.8)	$2.9 \pm {}^{0.6}_{0.1}$ (2.6–3.8)	SW
	$3.6 \pm {}^{2.0}_{0.6}$ (2.5–6.8)	$3.6 \pm {}^{0.4}_{0.4}$ (3.0–4.2)	NW
Lock850.3	$4.1 \pm {}^{2.3}_{0.6}$ (2.8–7.7)	$3.9 \pm {}^{0.6}_{0.4}$ (3.2–4.8)	S
	$3.1 \pm {}^{1.6}_{0.8}$ (2.0–6.1)	$2.6 \pm {}^{0.4}_{0.3}$ (2.2–3.2)	Co-added
Lock850.4	$2.1 \pm {}^{1.8}_{0.4}$ (1.5–5.8)	$2.1 \pm {}^{0.3}_{0.1}$ (1.8–3.1)	Co-added
Lock850.5	$\geqslant$2.9	$\geqslant$3.0	
Lock850.6	$4.1 \pm {}^{2.5}_{0.6}$ (3.0–8.0)	$3.6 \pm {}^{1.0}_{0.1}$ (2.8–4.8)	
Lock850.7	$3.1 \pm {}^{1.8}_{0.6}$ (2.0–6.3)	$2.9 \pm {}^{0.4}_{0.3}$ (2.2–3.4)	
Lock850.8	$\geqslant$2.5	$\geqslant$2.5	
Lock850.9	$2.1 \pm {}^{2.0}_{0.1}$ (1.5–5.8)	$2.4 \pm {}^{0.3}_{0.4}$ (2.0–3.2)	
Lock850.10	$3.4 \pm {}^{2.3}_{0.6}$ (2.2–7.0)	$3.1 \pm {}^{0.9}_{0.3}$ (2.8–4.7)	
Lock850.11	$\geqslant$2.2	$\geqslant$2.5	
Lock850.12	$2.6 \pm {}^{1.6}_{0.6}$ (1.5–6.2)	$2.6 \pm {}^{0.4}_{0.2}$ (2.2–3.8)	
Lock850.13	$\geqslant$1.5	$\geqslant$1.5	
Lock850.14	$\geqslant$2.2	$\geqslant$2.2	No 1.4 GHz[a]
Lock850.15	$2.6 \pm {}^{1.6}_{0.8}$ (1.2–5.9)	$2.4 \pm {}^{0.4}_{0.4}$ (2.0–3.2)	Co-added
	$3.1 \pm {}^{2.0}_{0.9}$ (1.8–6.8)	$2.9 \pm {}^{0.4}_{0.5}$ (2.2–3.8)	S
Lock850.16	$1.6 \pm {}^{1.3}_{0.4}$ (1.0–4.7)	$3.1 \pm {}^{0.1}_{0.7}$ (2.0–3.4)	
Lock850.17	$1.6 \pm {}^{1.2}_{0.4}$ (1.0–4.2)	$2.9 \pm {}^{0.3}_{0.4}$ (2.3–3.2)	
Lock850.18	$3.1 \pm {}^{2.1}_{0.6}$ (1.5–6.1)	$2.9 \pm {}^{0.4}_{0.5}$ (2.2–3.7)	
Lock850.19	$\geqslant$1.8	$\geqslant$1.5	
Lock850.21	$\geqslant$1.5	$\geqslant$1.0	
Lock850.22	$\geqslant$2.0	$\geqslant$2.0	
Lock850.23	$\geqslant$1.6	$\geqslant$1.5	
Lock850.24	$2.6 \pm {}^{1.2}_{1.1}$ (1.2–5.8)	$2.4 \pm {}^{0.4}_{0.3}$ (2.0–3.1)	
Lock850.26	$3.1 \pm {}^{1.9}_{1.1}$ (1.5–7.2)	$3.6 \pm {}^{0.1}_{0.8}$ (2.2–3.9)	
Lock850.27	$3.9 \pm {}^{1.9}_{1.1}$ (1.8–6.5)	$3.9 \pm {}^{1.9}_{1.1}$ (1.8–6.5)	
Lock850.28	$\geqslant$2.0	$\geqslant$2.0	
Lock850.29	$\geqslant$2.2	$\geqslant$2.1	
Lock850.30	$1.1 \pm {}^{0.8}_{0.4}$ (0.5–3.2)	$2.1 \pm {}^{0.1}_{0.4}$ (1.8–2.5)	
Lock850.31	$2.6 \pm {}^{1.9}_{0.6}$ (1.5–6.4)	$2.6 \pm {}^{0.1}_{0.6}$ (2.0–3.1)	
Lock850.33	$2.1 \pm {}^{1.4}_{0.6}$ (1.2–5.4)	$2.1 \pm {}^{0.7}_{0.4}$ (1.8–3.2)	
Lock850.34	$3.4 \pm {}^{1.6}_{1.0}$ (2.0–6.5)	$3.1 \pm {}^{0.6}_{0.2}$ (2.6–3.8)	
Lock850.35	$\geqslant$2.0	$\geqslant$2.0	
Lock850.36	$\geqslant$2.5	$\geqslant$2.5	
Lock850.37	$2.9 \pm {}^{1.6}_{1.1}$	$4.5 \pm {}^{1.0}_{0.3}$ (4.3–5.8)	N ($P = 0.013$)
	$3.9 \pm {}^{2.6}_{1.1}$	$4.6 \pm {}^{0.6}_{0.1}$ (4.5–5.8)	S (adopted $P = 0.078$)
Lock850.38	$2.6 \pm {}^{1.8}_{1.1}$ (0.8–6.2)	$2.1 \pm {}^{0.1}_{0\alpha.1}$ (2.0–2.3)	
Lock850.39	$\geqslant$2.2	$\geqslant$2.0	
Lock850.40	$2.6 \pm {}^{2.2}_{0.6}$ (1.2–6.3)	$2.6 \pm {}^{0.6}_{0.2}$ (2.0–3.2)	
Lock850.41	$2.1 \pm {}^{1.4}_{0.6}$ (1.2–5.3)	$3.6 \pm {}^{0.4}_{0.4}$ (2.5–4.0)	S
	$1.4 \pm {}^{1.4}_{0.1}$ (1.0–4.7)	$2.9 \pm {}^{0.5}_{0.1}$ (2.3–3.5)	N+S
Lock850.43	$3.6 \pm {}^{1.2}_{1.6}$ (1.5–6.6)	$2.4 \pm {}^{0.8}_{0.1}$ (2.2–3.8)	Adopted $P = 0.060$
Lock850.47	$\geqslant$1.2	$\geqslant$1.5	
Lock850.48	$2.1 \pm {}^{1.5}_{1.1}$ (0.5–5.7)	$2.4 \pm {}^{0.5}_{0.1}$ (2.1–3.0)	Adopted $P = 0.068$
Lock850.52	$2.1 \pm {}^{1.9}_{0.6}$ (0.5–5.5)	$2.1 \pm {}^{0.1}_{0.1}$ (1.9–2.2)	
Lock850.53	$\geqslant$1.5	$\geqslant$1.5	
Lock850.60	$\geqslant$1.2	$\geqslant$1.5	

Table 4 – *continued*

Object	$z_{\rm phot}^{\rm SA}$	$z_{\rm phot}^{\rm MC}$	Notes
Lock850.63	$2.6 \pm \frac{2.1}{0.6}$ (1.5–6.4)	$2.6 \pm \frac{0.4}{0.4}$ (2.1–3.2)	
Lock850.64	$\geqslant$1.6	$\geqslant$1.5	
Lock850.66	$\geqslant$1.5	$\geqslant$1.5	
Lock850.67	$\geqslant$1.0	$\geqslant$1.0	
Lock850.70	$\geqslant$1.0	$\geqslant$1.0	
Lock850.71	$1.6 \pm \frac{1.2}{0.6}$ (0.5–4.3)	$2.9 \pm \frac{0.1}{0.7}$ (2.0–3.2)	
Lock850.73	$2.1 \pm \frac{2.6}{0.2}$ (1.0–6.2)	$2.4 \pm \frac{0.1}{0.2}$ (2.0–2.5)	N
	$2.1 \pm \frac{1.4}{0.9}$ (0.7–5.2)	$2.1 \pm \frac{0.1}{0.1}$ (1.9–2.5)	Co-added
Lock850.75	$\geqslant$1.1	$\geqslant$1.2	
Lock850.76	$2.1 \pm \frac{1.8}{0.6}$ (0.8–5.5)	$2.1 \pm \frac{0.2}{0.1}$ (2.0–2.5)	
Lock850.77	$2.9 \pm \frac{1.7}{1.1}$ (2.8–6.9)	$2.6 \pm \frac{0.8}{0.1}$ (2.2–3.8)	S
	$1.5 \pm \frac{1.6}{0.4}$ (0.8–4.8)	$2.8 \pm \frac{0.4}{0.4}$ (2.0–3.2)	N+S
Lock850.78	$\geqslant$1.1	$\geqslant$1.5	
Lock850.79	$2.6 \pm \frac{2.2}{0.6}$ (1.2–6.3)	$2.4 \pm \frac{0.6}{0.1}$ (2.0–3.2)	Adopted $P = 0.064$
Lock850.81	$\geqslant$1.9	$\geqslant$2.0	
Lock850.83	$\geqslant$0.8	$\geqslant$1.5	
Lock850.87	$1.6 \pm \frac{1.0}{0.6}$ (0.8–4.0)	$2.4 \pm \frac{0.6}{0.1}$ (1.9–3.0)	
Lock850.100	$\geqslant$2.1	$\geqslant$2.0	

[a]This source has a robust 1.4 GHz association in the data set of Ivison et al. (2002), but it is below the robustness level adopted for the analysis in this paper, and thus we will make use of the 1.4 GHz photometry of Ivison et al. (2007) as an upper limit.

measured flux densities, some faint sources will be lost below the radio-detection threshold and may receive misleadingly low flux-density limits. These effects can be viewed as a systematic flux calibration offset with consequences as severe as those encountered in optical/infrared photometric-redshift estimation. While random 1.4-GHz calibration uncertainties of 5 per cent have been accounted for in the estimation of the photometric redshifts, a systematic flux-density offset could shift the redshift distribution significantly. In order to explore this possibility, we have applied a 10 per cent flux increase to the LH photometry and recalculated the photometric redshifts. The combined redshift distribution shifts its peak by ~ -0.25, and consequently the mean values of the SXDF and LH distributions are more consistent, increasing from 0.3 per cent (Section 2.1.3) to a 7 per cent probability according to a Mann–Whitney *U*-test. Some intrinsic variation on the distribution of redshifts between the fields is, however, to be expected (see below).

3.1.1 Comparison of the SHADES redshift distribution with galaxy formation models

van Kampen et al. (2005) studied four different galaxy formation models that yielded different redshift distributions and clustering properties for the sub-mm population expected to be found in a survey of the depth and area covered by SHADES: (α) a hydrodynamical model (Muanwong et al. 2002), that follows the evolution of dark-matter, gas, star-like particles and galaxy fragments, that has been coupled with the analytical form for redshift distribution of Baugh, Cole & Frenk (1996); (β) a simple merger model that identifies sub-mm galaxies with major mergers of massive galaxies; (γ) a phenomenological model (van Kampen 2004), which is based on *N*-body simulations that identify the sites of major mergers and has two modes of star formation, quiescent and bursting and (δ) a stable clustering model (Gaztañaga & Hughes 2001). Fig. 7 represents the theoretical redshift distributions of SHADES galaxies found in these models. This figure has been complemented with (ϵ) a semi-analytical model for the joint formation and evolution of spheroids and quasi-stellar objects (QSOs) (Granato et al. 2004; Silva et al. 2005); and (ζ) an alternative semi-analytic model of galaxy formation for sub-mm galaxies (Baugh et al. 2005).

Furthermore, to enable a more accurate discrimination between the above predictions, all the galaxy formation models in Fig. 7 account for the incompleteness of sources in the SHADES catalogue (Coppin et al. 2006). The models have also been convolved with a representative radio–mm–FIR photometric precision of $\sigma \sim 0.4$, which is intermediate between the measured uncertainties derived for the two techniques used in this paper.

We have made a comparison, via a KS test, of the observed redshift probability density distributions with those predicted from the above models. In each case, a KS statistic has been calculated that accommodates the 1σ uncertainty in the median redshift of the models due to field-to-field variations. A study of 25 simulations made for each of the four models analysed by van Kampen et al. (2005) demonstrates that the mean redshift of $\sim$60 SHADES-like sub-mm galaxies varies by $\delta\bar{z}$ (rms) $\approx$0.25–0.55. In part, these shifts can be explained by Poisson noise (estimated $\sigma \sim 0.1$–0.2 from the simulations). The models show, however, that there could also be a significant component in the field-to-field variations that arise from intrinsic redshift differences due to varying amounts of groups or protoclusters of galaxies along the line-of-sight. Thus, the differences found between the LH and SXDF areas, and between these and smaller, deeper surveys like GOODS-North, could be partially explained by this effect.

The results of the KS test suggest that only model (ϵ) is close to being formally acceptable, with an 87 per cent probability for the model to agree with the measured probability density distribution that includes SHADES sources with and without radio detections according to Solution (a). With only a small shift ($\delta z \sim -0.3$) in the distribution, model (ϵ) also qualitatively reproduces ($\sim$60 per cent

Table 5. Photometric redshifts for SHADES sources in the SXDF field based on the 850 μm and 1.4 GHz data and 450 μm upper limits, and when significant, complemented with *Spitzer* photometry at 70 and 160 μm. Columns are as in Table 4.

Object	$z_{\rm phot}^{\rm SA}$	$z_{\rm phot}^{\rm MC}$	Notes
SXDF850.1	$2.9 \pm {}^{2.0}_{0.6}$ (1.8–6.3)	$2.6 \pm {}^{0.4}_{0.3}$ (2.2–3.4)	
SXDF850.2	$2.4 \pm {}^{0.8}_{1.1}$ (1.0–4.8)	$1.9 \pm {}^{0.4}_{0.1}$ (1.8–2.9)	
SXDF850.3	$2.4 \pm {}^{1.5}_{0.6}$ (1.5–5.9)	$2.1 \pm {}^{0.3}_{0.1}$ (2.0–2.6)	
SXDF850.4	$1.1 \pm {}^{1.0}_{0.4}$ (0.5–3.4)	$2.1 \pm {}^{0.4}_{0.2}$ (1.8–2.7)	
SXDF850.5	$1.4 \pm {}^{0.6}_{0.5}$ (0.5–2.8)	$1.4 \pm {}^{0.4}_{0.4}$ (0.6–2.0)	70, 160 μm included
SXDF850.6	$2.4 \pm {}^{1.9}_{0.6}$ (1.3–6.0)	$2.4 \pm {}^{1.2}_{0.1}$ (2.1–3.8)	NW
	$2.9 \pm {}^{1.6}_{0.9}$ (1.5–6.0)	$2.6 \pm {}^{0.4}_{0.4}$ (2.2–3.7)	N
SXDF850.7	$2.4 \pm {}^{2.1}_{0.5}$ (1.8–6.6)	$2.4 \pm {}^{0.5}_{0.1}$ (2.2–3.4)	
SXDF850.8	$2.4 \pm {}^{1.6}_{0.6}$ (1.2–5.8)	$2.6 \pm {}^{1.3}_{0.1}$ (2.3–4.0)	
SXDF850.9	$\geqslant$1.8	$\geqslant$1.5	
SXDF850.10	$1.4 \pm {}^{1.5}_{0.1}$ (0.8–4.6)	$2.6 \pm {}^{0.3}_{0.6}$ (1.9–3.2)	
SXDF850.11	$1.9 \pm {}^{1.5}_{0.6}$ (1.0–5.6)	$2.4 \pm {}^{0.4}_{0.4}$ (2.0–3.4)	
SXDF850.12	$1.9 \pm {}^{2.4}_{0.1}$ (1.2–6.3)	$2.4 \pm {}^{0.3}_{0.4}$ (2.0–3.0)	
SXDF850.14	$2.4 \pm {}^{1.6}_{0.9}$ (1.2–6.3)	$2.4 \pm {}^{0.4}_{0.3}$ (2.0–3.1)	
SXDF850.15	$\geqslant$1.8	$\geqslant$2.0	
SXDF850.16	$2.4 \pm {}^{1.9}_{0.6}$ (1.2–6.2)	$2.4 \pm {}^{0.6}_{0.2}$ (2.0–3.2)	
SXDF850.17	$\geqslant$2.0	$\geqslant$2.0	
SXDF850.18	$2.4 \pm {}^{2.0}_{0.6}$ (1.5–6.1)	$2.9 \pm {}^{0.2}_{0.6}$ (2.2–3.7)	
SXDF850.19	$1.6 \pm {}^{1.1}_{0.6}$ (0.8–4.6)	$2.4 \pm {}^{0.4}_{0.4}$ (2.0–3.2)	
SXDF850.20	$\geqslant$1.4	$\geqslant$1.5	
SXDF850.21	$0.6 \pm {}^{0.9}_{0.2}$ (0.0–2.2)	$0.5 \pm {}^{0.4}_{0.2}$ (0.0–1.2)	70, 160 μm included
SXDF850.22	$\geqslant$1.8	$\geqslant$2.0	
SXDF850.23	$1.9 \pm {}^{1.4}_{0.6}$ (1.0–5.0)	$2.4 \pm {}^{0.9}_{0.2}$ (2.0–3.5)	
SXDF850.24	$2.4 \pm {}^{1.6}_{0.9}$ (1.1–6.0)	$2.4 \pm {}^{0.6}_{0.1}$ (2.2–3.7)	
	$2.9 \pm {}^{1.5}_{1.1}$ (1.5–6.8)	$2.9 \pm {}^{0.1}_{0.6}$ (2.2–3.7)	S
SXDF850.25	$\geqslant$1.0	$\geqslant$1.0	
SXDF850.27	$1.1 \pm {}^{0.9}_{0.5}$ (0.5–3.3)	$3.6 \pm {}^{0.1}_{0.8}$ (2.4–3.8)	
SXDF850.28	$1.6 \pm {}^{1.1}_{0.4}$ (0.5–4.4)	$1.4 \pm {}^{0.5}_{0.5}$ (0.6–2.2)	N, 70, 160 μm included
	$1.2 \pm {}^{1.1}_{0.4}$ (0.2–3.2)	$1.1 \pm {}^{0.4}_{0.1}$ (0.5–1.5)	N+S
SXDF850.29	$1.1 \pm {}^{0.9}_{0.4}$ (0.6–3.5)	$2.1 \pm {}^{0.1}_{0.3}$ (1.8–2.4)	
SXDF850.30	$2.9 \pm {}^{1.8}_{1.1}$ (1.2–6.8)	$2.9 \pm {}^{0.2}_{0.6}$ (2.2–3.8)	
SXDF850.31	$2.1 \pm {}^{1.6}_{0.6}$ (1.5–6.1)	$2.6 \pm {}^{0.5}_{0.4}$ (2.2–3.7)	
SXDF850.32	$\geqslant$1.5	$\geqslant$1.5	
SXDF850.35	$2.4 \pm {}^{1.6}_{0.9}$ (1.2–6.2)	$2.4 \pm {}^{0.6}_{0.1}$ (2.1–3.2)	
SXDF850.36	$\geqslant$1.8	$\geqslant$2.0	
SXDF850.37	$2.1 \pm {}^{2.1}_{0.5}$ (0.8–5.9)	$2.1 \pm {}^{0.1}_{0.1}$ (2.0–2.4)	
SXDF850.38	$1.9 \pm {}^{1.8}_{0.6}$ (0.3–5.0)	$1.9 \pm {}^{0.2}_{0.1}$ (1.7–2.2)	
SXDF850.39	$\geqslant$1.2	$\geqslant$1.5	
SXDF850.40	$2.1 \pm {}^{1.9}_{0.6}$ (1.0–5.8)	$2.4 \pm {}^{0.4}_{0.4}$ (2.0–3.2)	
SXDF850.45	$\geqslant$2.8	$\geqslant$3.0	
SXDF850.47	$1.1 \pm {}^{0.8}_{0.6}$ (0.2–3.1)	$1.9 \pm {}^{0.3}_{0.1}$ (1.6–2.2)	NE
	$2.1 \pm {}^{1.4}_{1.0}$ (0.6–5.2)	$2.1 \pm {}^{0.1}_{0.1}$ (1.9–2.2)	SE
	$1.1 \pm {}^{0.7}_{0.6}$ (0.2–2.9)	$1.6 \pm {}^{0.3}_{0.1}$ (1.5–2.1)	NE+SE
	$1.6 \pm {}^{1.3}_{0.6}$ (0.5–4.4)	$2.1 \pm {}^{0.1}_{0.2}$ (1.8–2.4)	W
SXDF850.48	$\geqslant$1.8	$\geqslant$2.0	
SXDF850.49	$\geqslant$0.5	$\geqslant$1.0	

Table 5 – *continued*

Object	$z_{\rm phot}^{\rm SA}$	$z_{\rm phot}^{\rm MC}$	Notes
SXDF850.50	$2.4 \pm {}^{2.0}_{0.9}$ (1.2–6.6)	$2.9 \pm {}^{0.1}_{0.6}$ (2.2–3.6)	
SXDF850.52	$1.6 \pm {}^{1.1}_{0.6}$ (0.5–4.1)	$2.1 \pm {}^{0.1}_{0.2}$ (1.6–2.2)	E
	$1.1 \pm {}^{0.9}_{0.6}$ (0.2–3.1)	$2.1 \pm {}^{0.1}_{0.4}$ (1.5–2.2)	ES
SXDF850.55	$2.4 \pm {}^{1.6}_{1.1}$ (0.5–5.6)	$2.1 \pm {}^{0.1}_{0.2}$ (1.8–2.2)	
SXDF850.56	$\geqslant$0.6	$\geqslant$1.0	
SXDF850.63	$\geqslant$1.0	$\geqslant$1.0	
SXDF850.65	$\geqslant$1.2	$\geqslant$1.5	
SXDF850.69	$\geqslant$0.8	$\geqslant$1.0	
SXDF850.70	$\geqslant$1.0	$\geqslant$1.0	
SXDF850.71	$\geqslant$0.8	$\geqslant$1.0	
SXDF850.74	$2.1 \pm {}^{1.6}_{1.1}$ (0.9–5.8)	$2.1 \pm {}^{0.1}_{0.2}$ (1.8–2.2)	
SXDF850.76	$\geqslant$1.2	$\geqslant$1.5	
SXDF850.77	$2.1 \pm {}^{1.0}_{0.6}$ (1.0–6.0)	$2.1 \pm {}^{0.1}_{0.1}$ (1.8–2.2)	70, 160 μm included
SXDF850.86	$\geqslant$1.0	$\geqslant$1.0	
SXDF850.88	$\geqslant$1.0	$\geqslant$1.0	
SXDF850.91	$\geqslant$1.0	$\geqslant$1.5	
SXDF850.93	$\geqslant$0.8	$\geqslant$0.5	
SXDF850.94	$\geqslant$1.2	$\geqslant$1.5	
SXDF850.95	$\geqslant$1.0	$\geqslant$1.0	
SXDF850.96	$2.4 \pm {}^{1.8}_{0.9}$ (1.0–6.1)	$2.4 \pm {}^{0.6}_{0.1}$ (2.2–3.5)	
SXDF850.119	$2.2 \pm {}^{1.8}_{1.4}$ (0.0–4.5)	$1.9 \pm {}^{0.1}_{0.5}$ (1.2–2.2)	70, 160 μm included

probability of similarity) the photometric-redshift distribution of the radio-detected SHADES galaxies.

The SHADES sources in our analysis that are not detected at radio wavelengths have very flat redshift probability distributions, which simply places them at $z \gtrsim 1.0$, and hence these SHADES sources could also produce a secondary peak in the redshift distribution. In the ranking of similarities of measured and model distributions, models (α) and (γ), ∼45 per cent probability, have double peaks and are broader than the observed distributions. A different prior, that optimizes the redshift distribution of the SHADES sources without radio detections, could bring them closer to a level of formal acceptance. Finally, models (δ), (ζ) and (β) are all rejected with probabilities of <2 per cent of being consistent with the range of solutions depicted in Fig. 7.

3.2 The FIR luminosity of SHADES sources

The catalogues of redshifts presented in Tables 1–5 are an initial step towards characterizing the FIR luminosities and star formation rates (SFRs) of the SHADES population. The available photometry in the FIR peak regime (70–450 μm), however, is not deep enough to fully constrain the SEDs of most SHADES sources at these wavelengths. One viable approach is to use the 20 SEDs in our local template catalogue to derive the corresponding FIR luminosities from the 850 μm flux densities, bearing in mind that the lack of constraints at short wavelengths will dominate the errors in luminosity estimation over those of redshift (e.g. Hughes et al. 2002). Alternatively, one could use the 1.4 GHz radio flux density to deduce FIR luminosities via the radio–FIR luminosity correlation that characterizes the sub-mm galaxy population, since this now has been extended to $z \sim 0.5$–4 (Kovács et al. 2006). This latter approach has the advantage of providing mean FIR luminosities which are accurate for the bulk of the population, reducing the uncertainties in luminosity primarily to the accuracy of the photometric redshifts. However, the normalization of the relation might be shifted from the local *IRAS* correlation, and this could affect the FIR luminosities derived, and the comparison of these to nearby galaxies.

Regardless of this complication, the observed 1.4 GHz flux densities have been converted to rest-frame 1.4 GHz flux densities using a mean synchrotron radio slope of index $\alpha = -0.7$, and the monochromatic 1.4 GHz luminosity has been inferred using the photometric-redshift solution for each source. This is converted to FIR luminosity using the linear relationship $\log(L_{\rm FIR}/L_{1.4\,\rm GHz}/4.52\,\rm THz) = 2.14 \pm 0.07$ (Kovács et al. 2006). For each source, we have considered the effect of the uncertainties in redshift, 1.4 GHz flux and the reported scatter in the sub-mm galaxy FIR–radio correlation (Kovács et al. 2006) by bootstrapping 1000 times on the measured errors. For the 69 radio-detected SHADES sources in the LH and SXDF fields, the median FIR luminosity is $2.6 \times 10^{12}\,\rm L_\odot$, with a high-luminosity tail that extends to $1 \times 10^{13}\,\rm L_\odot$ (see Fig. 8). The distribution of luminosities for sources in both the LH and SXDF fields is similar.

The effect of non-radio-detected sources, which have very unconstrained and possibly high redshifts (Section 2.1), has also been considered by scaling a simple grey body of temperature $T = 35$ K and emissivity index $\beta = 1.5$, the average of a parametrized SED of the short sub-mm wavelength-detected SCUBA galaxies that define the radio–FIR correlation at $z \sim 1$–3 (Kovács et al. 2006) to the observed 850 μm flux density. The errors in the 850 μm flux density have been taken into account by bootstrapping on the inferred de-boosted distributions of 850 μm flux densities for each source, and the redshift has been selected at random between their 90 per cent lower limits (Tables 4 and 5) and, arbitrarily, $z = 5$. The resulting combined distribution has a median FIR luminosity of $2.6 \times 10^{12}\,\rm L_\odot$, the same as the distribution of radio-detected sources.

If one returns to the alternative approach of using the combination of 20 SEDs with the de-boosted 850 μm flux densities to derive the FIR luminosities, one derives a broader luminosity distribution than that depicted in Fig. 8, reflecting the wide variety of acceptable SED templates, with a median luminosity that is increased by ∼40 per cent.

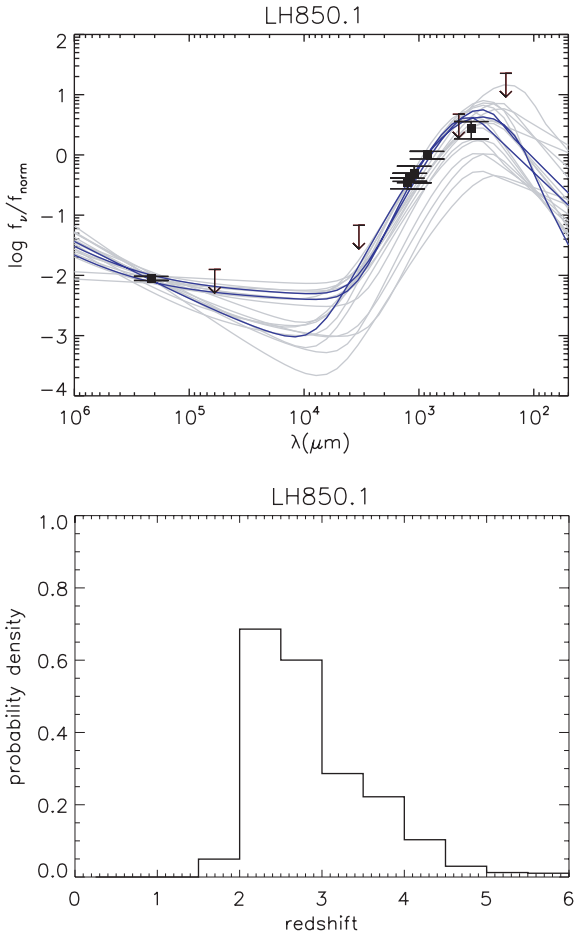

Figure 5. Top: SED of LH850.1, where the black squares mark detections, with 1σ error bars, and arrows indicate 3σ upper limits. For reference, the SED templates used in the photometric-redshift calculation are shifted to $z_{\rm A}^{\rm MC} = 2.4$ and scaled to maximize the likelihood function of detections and upper limit through survival analysis (Isobe et al. 1986), and are represented as lines. The SEDs compatible within the 3σ error bars of the photometry of the source are represented in darker (blue) lines. Bottom: probability distribution of LH850.1 derived for the $z_{\rm A}^{\rm MC}$ solution.

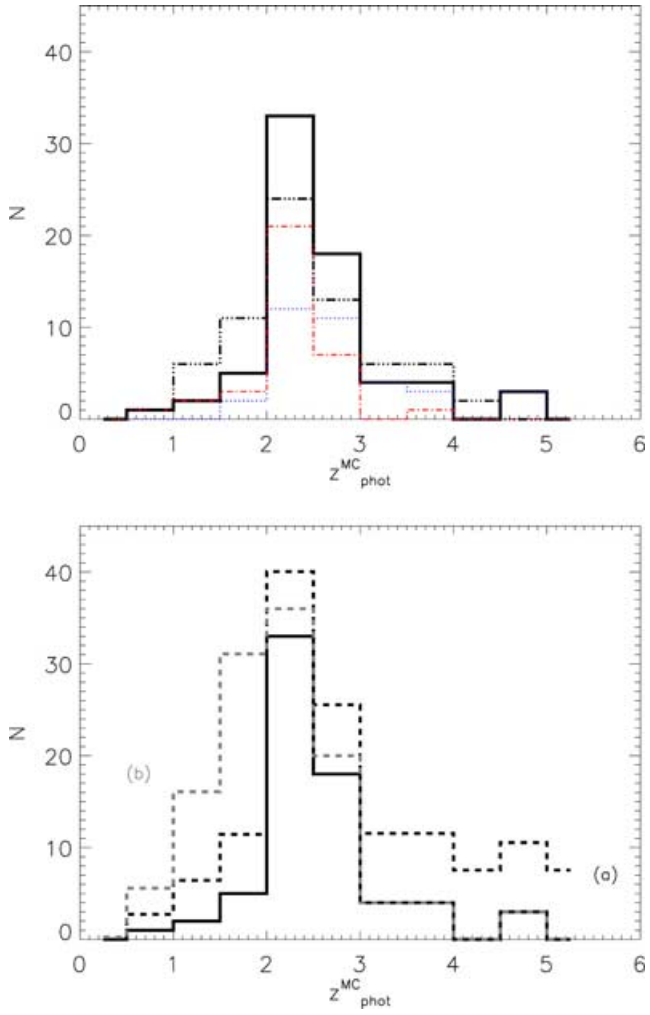

Figure 6. Histogram of the modes of the photometric redshifts of SHADES galaxies based on all available radio–mm–FIR photometry (provided in Table 3, or otherwise in Tables 4 and 5). Upper panel: the thick solid line (also shown in the lower panel) represents the $z_{\rm phot}^{\rm MC}$ distribution of modes for those 70 SCUBA galaxies that have been detected in at least two bands, of which the thin (blue) dotted line and thin (red) dash–dotted line represent the distributions defined by the LH and SXDF sources, respectively. For comparison, we plot the $z_{\rm phot}^{\rm SA}$ solutions for the full distribution of LH and SXDF (dash–dotted line). Lower panel: the black dashed line (a) and grey dashed line (b) show the redshift distributions for the 70 SCUBA galaxies detected in at least two bands, plus an additional 50 SCUBA galaxies detected only at 850 μm. These latter sources are distributed in one of two ways that bracket the range of reasonable options: (a) with equal probability between their calculated lower 90 per cent confidence limits and $z = 5$ and, alternatively, (b) between their lower limits and $z = 2$, or only at their lower redshift limits in the cases that these lie at $z > 2$.

3.3 The SFR history derived from SHADES galaxies

The evolution of the global SFR density traced by SHADES sources is shown in Fig. 9. The conversion from FIR luminosity to SFR was performed using a constant of $5 \times 10^9\,{\rm L}_\odot/({\rm M}_\odot\,{\rm yr}^{-1})$, which is constrained to $\sim \pm$ 30 per cent uncertainty (Kennicutt 1998). We have multiplied the contribution of each source to the star formation density by the inverse of the SHADES survey completeness function at the appropriate flux density (Coppin et al. 2006). Redshift space was binned into six intervals, and a MC was performed to assign each galaxy to a redshift bin according to its expected photometric-redshift error. The FIR luminosities have been estimated from the radio–FIR correlation or with a single SED which is considered to be representative of the sub-mm galaxy population (as in Section 3.2). The error bars in SFR density are the result of the uncertainties in photometry, SEDs and redshift, and are computed as the standard deviation traced by 1000 MC simulations.

The evolution in the SFR density traced by the radio-detected sources shows a clear peak at $z \sim 2.5$ and a slow decline at both low and high redshifts. A good description of the SFR density traced by this population is given by $\dot{\rho}_{\rm SF} \approx 0.35 \exp\left[-0.5(z-2.8)^2/(0.8^2)\right]$.

The contribution of non-radio-detected SHADES sources to the SFR history may be significant at high redshifts compared to the radio-detected SHADES sources, as indicated in Fig. 9 by the empty black diamonds [Solution (a) in Fig. 6]. Since the redshifts of these sources are not well constrained, this should be considered as only a possible evolutionary history, awaiting confirmation by better multiwavelength data to improve the constraints on the redshifts of the radio-undetected SHADES sources. The effect of placing all the radio-undetected sources between their lower redshift limits and $z = 2$ or at their lower limits if they are at $z > 2$ (Solution

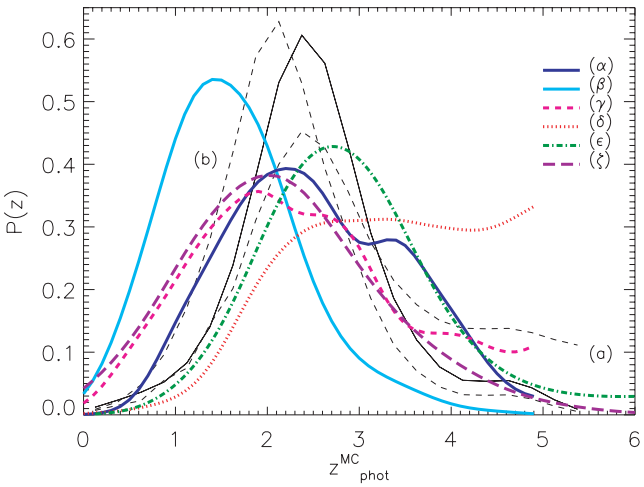

Figure 7. Probability density of the combined redshift distribution of SHADES galaxies [thin black solid line, and thin dashed lines (i and ii), as described in Fig. 6]. These are compared with the redshift distributions of six galaxy formation models (thick coloured lines), degraded with a $\sigma_z = 0.4$ to provide representative redshift uncertainties: (α) the hydrodynamical model of Muanwong et al. (2002) coupled with the analytical form for redshift distribution of Baugh, Cole & Frenk (1996); (β) the simple merger model of van Kampen et al. (2005); (γ) the phenomenological model of van Kampen (2004) and van Kampen et al. (2005); (δ) the stable clustering model of Gaztañaga & Hughes (2001); (ϵ) the semi-analytical model for the joint formation and evolution of spheroids and QSOs of Silva et al. (2005) and (ζ) the semi-analytic model for galaxy formation of Baugh et al. (2005).

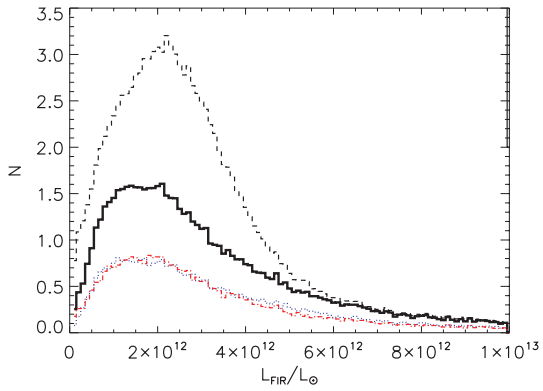

Figure 8. Distribution of FIR luminosities of the 120 SCUBA galaxies in the SHADES catalogue. The solid line represents the total distribution of radio-detected sub-mm sources in the two fields towards the LH (thin blue dotted line) and SXDF (thin red dash–dotted line) based on the FIR–radio correlation of sub-mm galaxies (Kovács et al. 2006). The dashed line shows the complete distribution of FIR luminosities for all SHADES sources, including the 51 non-radio-detected sub-mm sources, where the FIR luminosities of the latter sources have been derived from a single $T = 35$ K, $\beta = 1.5$ grey body scaled to the observed 850 μm flux density, and their redshifts have been selected at random between their lower 90 per cent confidence redshift limits and, arbitrarily, $z = 5$.

(b) in Fig. 6) is shown by the grey empty diamonds in Fig. 9, which understandably broadens the peak of star formation density to lower z.

The levels of star formation deduced for SHADES sources are consistent with those derived for other samples of radio-detected sub-mm galaxies at $z \leqslant 3.5$ (Chapman et al. 2005). At higher redshifts, however, the SFR densities implied in this photometric-redshift study exceed the extrapolations of Chapman et al. Eventually, spectroscopic measurements of SHADES sources at $z > 3.5$, via millimetre-wavelength observations of molecular CO lines, or optical spectroscopy with increased sensitivity, will provide a definitive measurement of the SFR density of obscured galaxies in the high-redshift Universe.

In order to estimate the contribution to the global SFR density of 850 μm sources that are fainter than those detected by SHADES, we have adopted the 60 μm luminosity function with a pure luminosity evolution that follows $(1 + z)^3$ at $z \leqslant 2$, and then maintains a constant level for $z > 2$. This evolutionary form provides an adequate description of the 850 μm and 1.1 mm counts (e.g. Scott et al. 2002; Greve et al. 2004) and is also supported up to $z = 1$ by the evolution of the luminosity function of 24 μm selected galaxies (Le Floc'h et al. 2005). By implementing this luminosity-function correction, the SFR density increases up to a maximum factor of 2 at $z > 2$.

The contribution of SHADES galaxies to the global SFR density of the Universe is comparable to the contribution of starbursts selected at optical/ultraviolet (UV) wavelengths at $1 \lesssim z \lesssim 4$ before the latter are corrected for dust extinction. It is important to recall that the L_{FIR}/SFR factor we have adopted could be in error by $\sim \pm 30$ per cent, and that SED differences could also account for an increase of ∼40 per cent. These uncertainties have not been carried into the estimation of error bars in Fig. 9. If we complete the luminosity function of SHADES galaxies towards lower luminosities, the FIR star formation rate traced by ultraluminous starbursts is still a factor of 1.2 to 2 lower than that of optical/UV starbursts that have been corrected for intrinsic dust extinction.

The recent demonstration that the contribution of luminous and ultraluminous IR galaxies dominates the SFR density at $z \leqslant 1$ (Le Floc'h et al. 2005) suggests that even if we correct for the incomplete sampling of the sub-mm galaxy luminosity function, a bright SHADES sub-mm survey could be missing the integrated contribution of dusty starbursts to the global SFR by a large factor (as high as ∼7), and thus dusty starbursts could indeed prove to be a significant mode of the star formation of the Universe (Blain et al. 1999).

The contribution of the fainter (<3 mJy) 850 μm sub-mm galaxy population to the star formation history of the Universe at $z > 1$ remains unconstrained at present, since detecting faint sub-mm galaxies has been restricted to a few strongly lensed fields (e.g. Smail, Ivison & Blain 1997) and extremely deep confusion-limited pencil observations (e.g. Hughes et al. 1998). Our estimations presented in Fig. 9 should therefore be considered an educated estimate of how ultraluminous IR–sub-mm galaxies trace the star formation history of the Universe.

Accurate measurements of the surface density and redshift distribution of the entire sub-mm galaxy population (and the faintest galaxies in particular) that contribute the complete sub-mm to FIR extragalactic background require deeper and larger mm and sub-mm surveys than are currently possible. The anticipated continuum and spectroscopic surveys with SCUBA-2 (Holland et al. 2006), the Large Millimetre Telescope (LMT; Serrano Pérez-Grovas et al. 2006) and the Atacama Large Millimetre Array (ALMA; Beasley, Murowinski & Tarenghi 2006), for example, will provide suitable data. In the meantime, however, it is still possible that the redshift distribution of the more populous and fainter (possibly extremely high redshift or alternatively less luminous) sub-mm galaxies is significantly different to those galaxies identified in the SHADES survey.

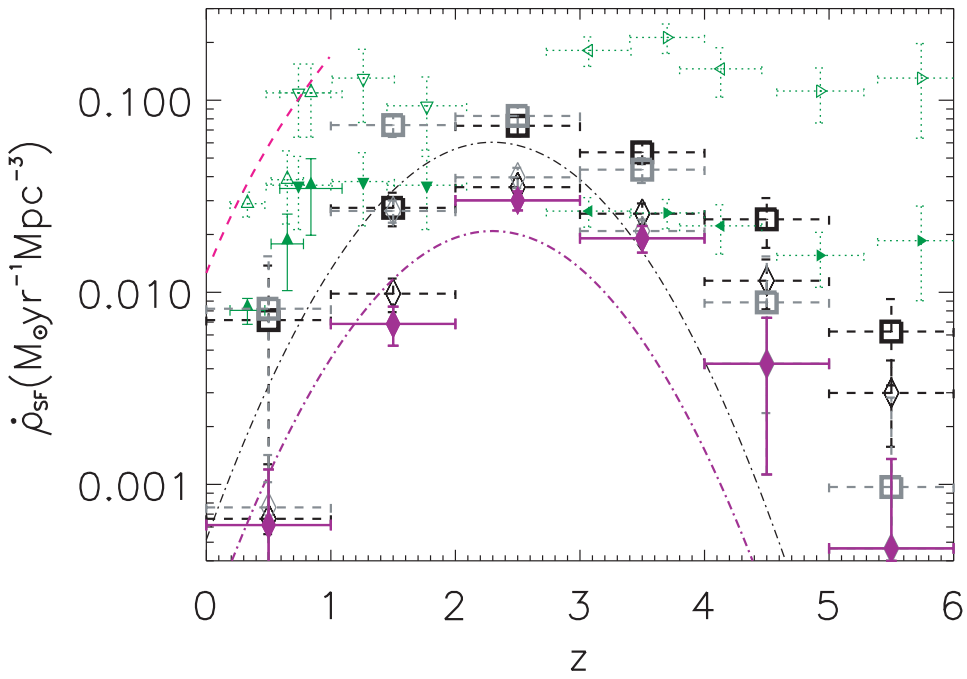

Figure 9. Evolution of the global star formation rate density (SFRD) for different samples of galaxies. We show the SFRD for radio-detected SHADES sources (solid diamonds) and for all SHADES galaxies, considering both the radio-detected and radio-undetected sources (open diamonds). The redshift probability distributions for the radio-undetected sources have been assumed to be flat between their lower redshift limits (Tables 4 and 5) and $z = 2$ (grey open diamonds) and $z = 5$ (black open diamonds). The redshift error bars indicate the width of the redshift bins. The error bars in $\dot{\rho}_{SF}$ are a combination of the uncertainty in the photometry, the recovery of the luminosity of each source due to SED differences and the uncertainty in redshift that divides the contribution of sources across several redshift bins (see Section 3.3). The empty square grey/black symbols represent the SFRD traced by ultraluminous 850-μm-selected starbursts by correcting the SFRDs derived for SHADES galaxies via the completion of the *IRAS* 60 μm luminosity function with pure luminosity evolution up to $z = 2$ (Section 3.3). The (pink) dashed line shows the SFRD inferred from 24 μm selected luminous and ultraluminous infrared galaxies (Le Floc'h et al. 2005), which follow a similar luminosity evolution to that presented here for the SHADES galaxies. The (purple) thick dash–dotted line shows the SFRD for the sample of SCUBA galaxies from Chapman et al. (2005). The thin dash–dotted line, which is a factor of ∼3 higher, is an estimation of the contribution of 850 μm selected galaxies down to the ∼1 mJy level. The SFRDs for optical/UV-selected starbursts are shown as small triangles, and are taken from Lilly et al. (1996, upward-pointing triangles), Connolly et al. (1997, downward-pointing), Steidel et al. (1999, left-pointing) and Giavalisco et al. (2004, right-pointing). The optical/UV data are shown with and without corrections for dust obscuration as empty and solid triangles, respectively, and all data have been homogenized to the same set of parameters and corrected to complete a Schechter luminosity function (Giavalisco et al. 2004). All estimates have been converted to the same SFR/L_{IR} factor and cosmological model described in Section 1.

4 SUMMARY OF CONCLUSIONS

(i) We have derived the photometric-redshift distribution of SHADES sources with de-boosted 850 μm flux densities > 3 mJy towards the LH and the SXDF using rest-frame radio-to-FIR photometry. The redshift distribution of the radio-detected sub-mm sources peaks at $z \sim 2.4$ with 50 per cent of the population between redshifts 1.8 and 3.1.

(ii) The combined redshift distribution of SHADES sources with robust radio counterparts, ∼60 per cent of the population, has a distribution which is qualitatively consistent with the distribution of rest-frame UV-optical spectroscopic redshifts published by Chapman et al. (2005).

(iii) We find a small ($\delta z \approx 0.5$), but significant, difference between the peaks of the photometric-redshift distributions of the LH and SXDF, which can be attributed to differences in the sensitivities of their respective radio maps. Intrinsic field-to-field redshift variance is also expected and is characterized according to a variety of models ($\delta z \approx 0.25$–0.55). This drives us to the conclusion that the incomplete area (∼720 arcmin^2) observed by SCUBA, despite being the largest sub-mm survey to date, may still be too small to be a representative sample of the bright sub-mm galaxy population.

(iv) The complete redshift distribution of all SHADES sources, including those sub-mm sources without detections at radio wavelengths (for which we adopt a variety of possibilities that describe their unconstrained distribution of redshifts) still maintains the peak (mode) of the bright sub-mm galaxy redshift distribution at ≈2.4. We have considered a variety of priors that describe the unconstrained redshift distributions of the sub-mm sources without radio detections. In the most extreme solutions, distributing these sources with equal probability between their lower redshift limit and $z = 2$ or 5, the bulk of the sub-mm population (50 per cent interquartile) lies in the range $1.6 \leqslant z \leqslant 2.6$ or $2.1 \leqslant z \leqslant 3.4$, respectively.

(v) The combined SHADES LH and SXDF redshift probability density distribution is compatible, within the uncertainties of our analysis, with the semi-analytical model for the joint formation of spheroids and QSOs of Granato et al. (2004) and Silva et al. (2005). If sources detected only at 850 μm are also introduced into the redshift probability density, with other priors than those illustrated here, then the hydrodynamical model of Muanwong et al. (2002) and phenomenological model of van Kampen (2004) and van Kampen et al. (2005) could also be in agreement with the observations. These compatible models, which are physically quite distinct, predict different clustering properties for the SHADES galaxies that could allow further discrimination between them (van Kampen et al. 2005). A detailed study of the clustering properties of SHADES galaxies will be the topic of a further paper.

(vi) The bright SHADES galaxies contribute to the SFR density of the Universe with $\sim$0.01 to 0.03 $M_\odot\,yr^{-1}\,Mpc^{-3}$ in the redshift interval $1 \lesssim z \lesssim 5$, and reach the levels of the dust-uncorrected Lyman Break Galaxy population (Giavalisco et al. 2004). The SFR density of dust-enshrouded starburst galaxies traced by ultraluminous SHADES galaxies, and completing the luminosity function to lower luminosity galaxies, is estimated to be a factor of 2 larger. This is still a factor of 1.2 to 2 lower than the optical/UV-selected starburst galaxy samples that include the latest dust-correction estimates. The current SHADES survey and complementary multiwavelength data, however, cannot characterize the bulk of the rest-frame FIR emission arising from these lower luminosity galaxies. A more statistically complete measurement of the universal history of star formation from powerful dusty, optically obscured galaxies awaits the commissioning of future large-aperture single-dish and interferometric submillimetre and millimetre telescopes targeting suitable extragalactic fields that have the necessary multiwavelength ancillary data.

ACKNOWLEDGMENTS

IA and DHH acknowledge partial support from Conacyt grants 39548-F and 39953-F and a Royal Society – Academia Mexicana de Ciencias 2005 exchange program. This work has also been partially funded by PPARC. KC acknowledges additional partial support from NSERC, IRS from the Royal Society, AJB from the Gordon and Betty Moore Foundation, MS from a Gary McCue Fellowship through the Center of Cosmology at UC Irvine and CS from a PPARC Advanced Fellowship.

REFERENCES

Almaini O., Dunlop J. S., Conselice C. J., Targett T. A., Mclure R. J., 2005, preprint (astro-ph/0511009)
Aretxaga I., Hughes D. H., Chapin E. L., Gaztañaga E., Dunlop J. S., Ivison R., 2003, MNRAS, 342, 759
Aretxaga I., Hughes D. H., Dunlop J. S., 2005, MNRAS, 358, 1240
Aretxaga I., Hughes D. H., Dunlop J. S., 2006, in Baker A. J., Glenn J., Harris A. I., Mangum J. G., Yun M. S., eds, From z-Machines to ALMA: (Sub)millimeter Spectroscopy of Galaxies. Astron. Soc. Pac., San Francisco, in press
Baugh C., Cole S., Frenk C. S., 1996, MNRAS, 282, 27
Baugh C. H., Lacey C. G., Frenk C. S., Granato G. L., Silva L., Bressan A., Benson A. J., Cole S., 2005, MNRAS, 356, 1191
Beasley A. J., Murowinski R., Tarenghi M., 2006, SPIE, 6267, 2
Blain A. W., Jameson A., Smail I., Longair M. S., Kneib J.-P., Ivison R. J., 1999, MNRAS, 309, 715
Blain A. W., Barnard V. E., Chapman S. C., 2003, MNRAS, 338, 733
Carilli C. L., Yun M. S., 1999, ApJ, 513, L13
Carilli C. L., Yun M. S., 2000, ApJ, 530, 618
Chapman S. C., Smail I., Ivison R. J., Blain A. W., 2002, ApJ, 335, L17
Chapman S. C., Blain A. W., Ivison R. J., Smail I. R., 2003, Nat, 422, 695
Chapman S. C., Blain A. W., Smail I., Ivison R. J., 2005, ApJ, 622, 772
Condon J. J., 1992, ARA&A, 30, 575
Connolly A. J., Szalay A. S., Dickinson M., Subbarao M. U., Brunner R. J., 1997, ApJ, 486, L11
Coppin et al., 2006, MNRAS, 372, 1621
Dunlop J. S., 2005, in de Grijs R., González Delgado R. M., eds, Astrophys. Space Sci. Library Vol. 329, Starbursts: From 30 Doradus to Lyman Break Galaxies. Springer, the Netherlands, p. 121
Dunne L., Clements D. L., Eales S. A., 2000, MNRAS, 319, 813
Greve T. R., Ivison R. J., Bertoldi F., stevens J. A., Dunlop J. S., Lutz D., Carilli C. L., 2004, MNRAS, 254, 779
Le Floc'h E. et al., 2005, ApJ, 632, 169
Gaztañaga E., Hughes D. H., 2001, in Lowenthal J. D., Hughes D. H., eds., Proc. UMass/INAOE Conf., Deep Millimeter Surveys: Implications for Galaxy Formation and Evolution. World Scientific, Singapore, p. 131
Giavalisco M. et al., 2004, ApJ, 600, L103
Granato G. L., De Zotti G., Silva L., Bressan A., Danese L., 2004, ApJ, 600, 580
Greve T. R. et al., 2005, MNRAS, 359, 1165
Heavens A., Panter B., Jiménez R., Dunlop J., 2004, Nat, 428, 625
Helou G., Soifer T., Rowan-Robinson M., 1985, ApJ, 298, L7
Holland W. S. et al., 1999, MNRAS, 303, 659
Holland W. S. et al., 2006, SPIE, 6275, 45
Hughes D. H. et al., 1998, Nat, 394, 241
Hughes D. H. et al., 2002, MNRAS, 335, 871
Hunt L. K., Maiolino R., 2005, ApJ, 626, L15
Ivison R. J. et al., 2002, MNRAS, 337, 1
Ivison R. J. et al., 2005, MNRAS, 364, 1025
Ivison R. J. et al., 2007, MNRAS, in press
Isobe T., Feigelson E. D., Nelson P. I., 1986, ApJ, 306, 490
van Kampen E., 2004, in Plionis M., ed., Multi-Wavelength Cosmology. Kluwer, Dordrecht, p. 117
van Kampen E. et al., 2005, MNRAS, 359, 469
Kennicutt R. C., 1998, ARA&A, 36, 189
Kovács A., Chapman S. C., Dowell C. D., Blain A. W., Ivison R. J., Smail I., Phillips T. G., 2006, ApJ, 650, 592
Laurent G. T. et al., 2005, ApJ, 623, 742
Laurent G. T., Glenn J., Egami E., Rieke G. H., Ivison R. J., Yun M. S., Aguirre J. E., Maloney P. R., 2006, ApJ, 643, 1
Lilly S. J., Le Fevre O., Hammer F., Crampton D., 1996, ApJ, 460, L1
Lonsdale C. J. et al., 2003, PASP, 115, 897
Mortier A. et al., 2005, MNRAS, 363, 563
Muanwong O., Thomas P. A., Kay S. T., Pearce F. R., 2002, MNRAS, 336, 527
Pope A., Borys C., Scott D., Conselice C., Dickinson M., Mobasher B., 2005, MNRAS, 358, 149
Pope A. et al., 2006, MNRAS, 370, 1185
Rengarajan T. N., Takeuchi T. T., 2001, PASJ, 53, 433
Scott S. et al., 2002, MNRAS, 331, 817
Serrano Pérez-Grovas A., Scholerb F. P., Hughes D. H., Yun M. S., 2006, SPIE, 6267, 1
Silva L., De Zotti G., Granato G. L., Maiolino R., Danese L., 2005, MNRAS, 357, 1295
Smail I., Ivison R. J., Blain A. W., 1997, ApJ, 490, L5
Steidel C. C., Adelberger K. L., Giavalisco M., Dickinson M., Peltini M., 1999, ApJ, 519, 1
Swinbank A. M., 2005, MNRAS, 359, 401
Yun M. S., Carilli C. L., 2002, ApJ, 568, 88
Yun M. S., Reddy N. A., Condon J. J., 2001, ApJ, 554, 803
Wiklind T., 2003, ApJ, 588, 736
Wilson G. W., Austermann J., Logan D. W., Yun M., 2004, SPIE, 5498, 246

This paper has been typeset from a TEX/LATEX file prepared by the author.